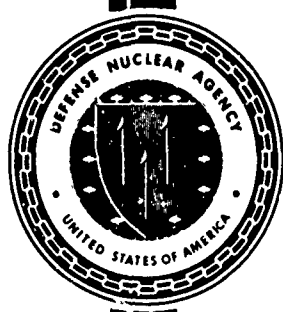


AD 74 4666



DNA 2716

29 February 1972

**NEUTRON SCATTERING AND  
GAMMA-RAY PRODUCTION  
CROSS SECTIONS FOR  
N, O, AI, Si, Ca, AND Fe**

**FINAL REPORT**

**HEADQUARTERS  
Defense Nuclear Agency  
Washington, D.C. 20305**

Contract No. DASA01-68-C-0128

**PREPARING AGENCY  
Nuclear-Chicago Corporation  
Texas Nuclear Division  
P.O. Box 9267  
Austin, Texas 78766**

Reproduced by  
**NATIONAL TECHNICAL  
INFORMATION SERVICE**  
U S Department of Commerce  
Springfield VA 22151

**APPROVED FOR PUBLIC RELEASE  
DISTRIBUTION UNLIMITED**

Destroy this report when it is no longer needed. Do not return to sender.

*[Handwritten mark]*

*[Handwritten mark]*

## Security Classification

14 KEY WORDS	LINK A		LINK B		LINK C	
	ROLE	WT	ROLE	WT	ROLE	WT
N, O, Al, Si, Ca, Fe Nuclear Data Neutron energy 9 and 11 MeV Neutron elastic cross section Neutron inelastic cross section Neutron induced gamma-ray production cross sections						

Security Classification

16

**DNW 2716**

**29 February 1972**

**NEUTRON SCATTERING AND  
GAMMA-RAY PRODUCTION  
CROSS SECTIONS FOR  
N, O, Al, Si, Ca, AND Fe**

**FINAL REPORT**

THIS WORK WAS SUPPORTED BY THE DEFENSE NUCLEAR AGENCY  
UNDER NWER SUBTASK XAXPC10104.

**D. O. Nellis and P. S. Buchanan, Authors**

**Defense Nuclear Agency  
Washington, D.C. 20305**

**Contract No. DASA01-68-C-0128**

**PREPARING AGENCY**

Nuclear-Chicago Corporation  
Texas Nuclear Division  
P.O. Box 9267  
Austin, Texas 78766

**Work done by:**  
D. O. Nellis, P. S. Buchanan  
T. C. Martin, W. E. Tucker  
G. H. Williams, A. J. Wolfram

**APPROVED FOR PUBLIC RELEASE  
DISTRIBUTION UNLIMITED**

*1c*

ABSTRACT

Measurements of neutron elastic and inelastic scattering and gamma-ray production have been made on several elements with 9.0 and 11.0 MeV incident neutrons. Differential cross sections for N, O, Al, Si, Ca and Fe are presented and integral cross sections derived from the data are also given.

TABLE OF CONTENTS

ABSTRACT.....	ii
1. INTRODUCTION.....	1
2. NEUTRON MEASUREMENTS.....	2
2.1 DATA ACQUISITION.....	2
2.2 DATA REDUCTION.....	7
2.3 RESULTS.....	9
3. GAMMA RAY MEASUREMENTS.....	17
3.1 DATA ACQUISITION.....	17
3.2 DATA REDUCTION.....	20
3.3 RESULTS.....	22
4. DISCUSSION.....	27
5. REFERENCES.....	90
6. APPENDIX (Errata for Report DASA-2333).....	93

## ILLUSTRATIONS

<u>Figure</u>	<u>Page</u>
1. Basic data acquisition system for neutron cross section work at LASL.....	28
2. Shielding geometry for neutron cross section work at LASL.....	29
3. Time-of-flight spectrum from the neutron monitor.....	30
4. Efficiency vs. energy for the NE-213 neutron detector.....	31
5. Spectra illustrating the effect of a $^{58}\text{Ni}$ beam stop.....	32
6. Nitrogen time-of-flight spectrum at $E_n = 9.0 \text{ MeV}$ .....	33
7. Nitrogen time-of-flight spectrum at $E_n = 11.0 \text{ MeV}$ .....	34
8. Oxygen time-of-flight spectrum at $E_n = 9.0 \text{ MeV}$ .....	35
9. Oxygen time-of-flight spectrum at $E_n = 11.0 \text{ MeV}$ .....	36
10. Aluminum time-of-flight spectrum at $E_n = 9.0 \text{ MeV}$ .....	37
11. Silicon time-of-flight spectrum at $E_n = 9.0 \text{ MeV}$ .....	38
12. Calcium time-of-flight spectrum at $E_n = 11.0 \text{ MeV}$ .....	39
13. Iron time-of-flight spectrum at $E_n = 9.0 \text{ MeV}$ .....	40
14. Nitrogen elastic scattering at $E_n = 9.0 \text{ MeV}$ .....	41
15. Nitrogen elastic scattering at $E_n = 11.0 \text{ MeV}$ .....	42
16. Oxygen elastic scattering at $E_n = 9.0 \text{ MeV}$ .....	43
17. Oxygen elastic scattering at $E_n = 11.0 \text{ MeV}$ .....	44
18. Aluminum elastic scattering at $E_n = 9.0 \text{ MeV}$ .....	45
19. Aluminum elastic scattering at $E_n = 11.0 \text{ MeV}$ .....	46
20. Silicon elastic scattering at $E_n = 9.0 \text{ MeV}$ .....	47

21.	Silicon elastic scattering at $E_n = 11.0$ MeV.....	48
22.	Calcium elastic scattering at $E_n = 9.0$ MeV.....	49
23.	Calcium elastic scattering at $E_n = 11.0$ MeV.....	50
24.	Iron elastic scattering at $E_n = 9.0$ MeV.....	51
25.	Iron elastic scattering at $E_n = 11.0$ MeV.....	52
26.	Gamma-ray spectrometer arrangement used at LASL.....	53
27.	Efficiency vs. energy for the gamma-ray spectrometer....	54
28.	Nitrogen gamma-ray spectrum at $E_n = 11.0$ MeV.....	55
29.	Aluminum gamma-ray spectrum at $E_n = 9.0$ MeV.....	56
30.	Calcium gamma-ray spectrum at $E_n = 9.0$ MeV.....	57

TABLES

<u>Table</u>	<u>Page</u>
1. Nitrogen elastic scattering at $E_n = 9.0$ MeV.....	58
2. Nitrogen elastic scattering at $E_n = 11.0$ MeV.....	59
3. Oxygen elastic scattering at $E_n = 9.0$ MeV.....	60
4. Oxygen elastic scattering at $E_n = 11.0$ MeV.....	61
5. Aluminum elastic scattering at $E_n = 9.0$ MeV.....	62
6. Aluminum elastic scattering at $E_n = 11.0$ MeV.....	63
7. Silicon elastic scattering at $E_n = 9.0$ MeV.....	64
8. Silicon elastic scattering at $E_n = 11.0$ MeV.....	65
9. Calcium elastic scattering at $E_n = 9.0$ MeV.....	66
10. Calcium elastic scattering at $E_n = 11.0$ MeV.....	67
11. Iron elastic scattering at $E_n = 9.0$ MeV.....	68
12. Iron elastic scattering at $E_n = 11.0$ MeV.....	69
13. Nitrogen inelastic scattering at $E_n = 9.0$ MeV.....	70
14. Nitrogen inelastic scattering at $E_n = 11.0$ MeV.....	71
15. Oxygen inelastic scattering to the 6.06 and 6.13 MeV levels at $E_n = 9.0$ MeV.....	72
16. Oxygen inelastic scattering to the 6.06 and 6.13 MeV levels at $E_n = 11.0$ MeV.....	73
17. Oxygen inelastic scattering to the 6.92 and 7.12 MeV levels at $E_n = 11.0$ MeV.....	74
18. Aluminum inelastic scattering at $E_n = 9.0$ MeV.....	75
19. Aluminum inelastic scattering at $E_n = 11.0$ MeV.....	76
20. Silicon inelastic scattering at $E_n = 9.0$ MeV.....	77
21. Silicon inelastic scattering at $E_n = 11.0$ MeV.....	78

<u>Table</u>	<u>Page</u>
22. Calcium inelastic scattering at $E_n = 9.0$ MeV.....	79
23. Calcium inelastic scattering at $E_n = 11.0$ MeV.....	80
24. Iron inelastic scattering at $E_n = 9.0$ MeV.....	81
25. Iron inelastic scattering at $E_n = 11.0$ MeV.....	82
26. Nitrogen gamma-ray production at $E_n = 11.0$ MeV.....	83
27. Oxygen gamma-ray production at $E_n = 11.0$ MeV.....	84
28. Aluminum gamma-ray production at $E_n = 9.0$ MeV.....	85
29. Aluminum gamma-ray production at $E_n = 11.0$ MeV.....	86
30. Calcium gamma-ray production at $E_n = 9.0$ MeV.....	87
31. Calcium gamma-ray production at $E_n = 11.0$ MeV.....	88
32. Iron gamma-ray production at $E_n = 9.0$ MeV.....	89

THIS PAGE IS INTENTIONALLY LEFT BLANK.

## 1. INTRODUCTION

Numerical values of neutron elastic and inelastic cross sections and gamma-ray production cross sections for N, O, Al, Si, Ca and Fe have been measured at neutron energies of 9 and 11 MeV. The work reported here represents essentially an extension of work accomplished previously under this contract.<sup>1</sup> Neutron measurements were made at laboratory angles between 30° and 125° whereas the gamma-ray measurements were made only at 55°. All data were obtained at the Tandem Accelerator Facility of the Los Alamos Scientific Laboratory. Data were accumulated in the laboratory's SDS Sigma 7 computer and stored on magnetic tape for future manipulation. Also, printouts and plots of the data were transported to the Texas Nuclear facility for data reduction and analysis.

Considerable help and advice were received from members of the LASL staff during the performance of these experiments. We extend our appreciation to the LASL staff and in particular would like to acknowledge the help of Phil Young, Graham Foster, Darrell Drake, John Hopkins and Jim Martin, especially in the early stages of the experiment; and of Dick Woods, Jules Levin and Martin Kellogg and many others for their continuous assistance during all stages of the work.

## 2. NEUTRON MEASUREMENTS

### 2.1 DATA ACQUISTION

Fig. 1 shows a simplified schematic diagram of the sample detector geometry and basic data acquisition system used in the experiment. The LASL tandem Van de Graaff was used to provide pulsed (2.5 MHz) and bunched ( $\approx$  1 nsec FWHM) bursts of protons to a tritium gas cell where neutrons were produced by the  $T(p,n)^3He$  reaction. The neutrons were detected with an organic scintillator detector incorporating neutron-gamma discrimination. Conventional time-of-flight techniques were used to improve background effects and to separate neutron groups.

The neutron detector consisted of a 12.5 cm diameter, 5 cm thick NE-213 liquid scintillator optically coupled to a 58 AVP photomultiplier connected to a Nuclear Enterprises NE 5553A pulse-shape discriminator assembly. The detector assembly was housed in a 2 inch thick lead sleeve surrounded by a massive borated polyethylene shield which could be rotated about the scattering sample. Fig. 2 shows the detector geometry and the additional shielding and shadow bars used to reduce the backgrounds. A gamma-ray absorber consisting of a 1.38 cm lead disc (shown directly in front of the liquid scintillator) was required to reduce the count rate in the detector.

Physical restrictions at the experimental site prevented

the use of long flight paths. The neutron flight path between the scattering sample and the detector was maintained at 220 cm throughout the experiment. The time resolution of the detector system for elastically scattered neutrons was of the order of 3 nsec or 1.5 MeV FWHM. Under these conditions it was not possible to resolve the inelastic neutrons scattered from the lowest excited states of aluminum or iron.

Measurements were made in good geometry with cylindrical scattering samples of about 2.5 cm diameter and 4 cm length. The detailed descriptions of the individual samples used are given in the discussion section. The neutron-source-to-sample distance used for the measurements was of the order of 10 cm.

The neutron flux incident on the scattering samples was monitored with both a neutron time-of-flight monitor and a proton-recoil telescope. The monitor consisted of a  $\frac{1}{2}$ " x  $\frac{1}{2}$ " plastic scintillator and photomultiplier used in conjunction with conventional time-of-flight electronics and was mounted at  $135^\circ$  above the target at a distance of 1 meter. A typical spectrum from the neutron monitor is shown in Fig. 3. The proton recoil telescope, based on the design of Bame et al.<sup>2,3</sup> was positioned at  $0^\circ$  to the incident beam, and subtended a half angle of  $1^\circ$  to the neutron target. Typical recoil-proton spectra obtained with this telescope can be found in the preceding contract progress report.<sup>1</sup>

The equivalent electron energy bias used on the NE-213 neutron detector was chosen at one third of the Compton edge for  $^{137}\text{Cs}$  or an energy of 220 keV. This corresponds to a neutron energy cut off of around 1 MeV. The efficiency curve and all measurements reported here were obtained using this bias. The detector efficiency was determined at a number of energies by scattering monoenergetic neutrons from hydrogenous samples of known composition. The incident monoenergetic neutron flux was measured directly at the sample position by means of a conventional proton recoil telescope. Neutrons incident on the detector were then determined from the kinematics of the  $(n,p)$  reaction. Fig. 4 shows the data points obtained and the efficiency curve used in the calculations of the cross section data. Data points were not taken using the direct beam since the counting rate was too high. The dispersion of the data points are such as to indicate the accuracy of the curve to be within  $\pm 5\%$  except in the region of the neutron cut off.

The tritium gas target consisted of a 3 cm long stain-less steel cell separated from the main vacuum system by a thin foil and filled to a gas pressure of 3 atm. Early measurements were made with the existing LASL target system which had a  $9.3 \text{ mg/cm}^2$  Mo target entrance foil and a 10 mil Au beam stop on the end of the target cell. The large number of low energy neutrons produced by the  $p,n$  reaction in the Au stop, however, interfered with the observation of the inelastically scattered neutrons and required a change in the target system. Early in the experimental

measurements the gold end cap was replaced by a  $^{58}\text{Ni}$  stop (which has a p,n threshold of 9.4 MeV), and the Mo entrance foil was also replaced with a 9.6 mg/cm<sup>2</sup>  $^{58}\text{Ni}$  foil. The new target system appreciably reduced the low energy neutron background. Fig. 5 shows the neutron spectrum from aluminum taken with the Au beam stop and with the  $^{58}\text{Ni}$  beam stop and illustrates the large improvements in the background effect achieved with the  $^{58}\text{Ni}$  stop.

The procedure used in making the measurements was to bombard the tritium gas target with a predetermined number of protons (observed as the integrated charge collected at the electrically isolated target). The incident proton energies used were 10 and 12 MeV which produced neutrons having mean energies of  $8.91 \pm .09$  MeV and  $10.95 \pm 0.09$  MeV in the forward direction. The spread in the energy of the neutrons is attributed to proton straggling in the entrance foil and to energy losses in traversing the gas cell. The time-of-flight data and monitor data accumulated during the run was stored in the Sigma 7 computer for later manipulation. Typical operating conditions consisted of an average beam current of 1  $\mu\text{A}$  of protons at 2.5 MHz on the target cell, yielding a neutron flux of about  $10^8$  neutrons/steradian/sec at  $0^\circ$ . Data runs were made first with the scattering sample in position and then with no sample in position. In addition, for the inelastic neutron measurements it was necessary to take an additional pair of data runs with helium in the gas target cell. These runs were to remove the effect of the low energy background neutrons which appear in the inelastic region of the detector time-of-flight spectrum.

Measurements for elastic scattering were made at a number of angles between  $30^{\circ}$  and  $125^{\circ}$  with an estimated angular error of  $\pm 1^{\circ}$ . Measurements were generally made at three angles with helium in the gas cell to enable analysis of the inelastic region of the spectra at more than one angle.

## 2.2 DATA REDUCTION

The data reduction process is generally straightforward and only a brief discussion will be given here. The process usually begins with the subtraction of a sample-out spectrum from a sample-in spectrum after normalizing to an equivalent neutron flux. For the inelastic analysis an additional subtraction of a sample-in minus sample-out spectrum with helium in the target cell is necessary as indicated in the previous section. The elastic and resolved inelastic peaks are then stripped visually from the difference spectrum, allowing for residual backgrounds or tails from closely adjacent peaks which might lie under the peaks of interest. The stripping procedure is subjective but estimates of the errors involved are included with the accepted value. The remaining portion of the spectrum where there are no well resolved peaks is treated like a continuum and analyzed in equal energy increments. The integrated counts in each of the resolved peaks and energy increments in the continuum are obtained and these are then converted into cross sections (mb./sr) by appropriate techniques.

The neutron flux incident on the scattering sample is determined from the proton-recoil telescope data. The telescope counts are corrected for the effect of sample absorption and telescope radiator-out background prior to converting them to neutrons/steradian by the conventional method.<sup>3</sup> From the flux just obtained and the target-to-scattering-sample distance, the neutron flux at the center of the scattering sample with the sample not in place

is then established. This mid-point no-sample flux is then converted into an effective average flux in the scatterer by correcting for the effect of sample attenuation using the method of Cranberg and Levin<sup>4</sup> and for anisotropy in the neutron yield from the T(p,n)<sup>3</sup>He reaction.<sup>5</sup> The nonelastic cross sections  $\sigma_{ne}$  were used in the attenuation calculations rather than total cross sections  $\sigma_T$  since single elastic events neither appreciably degrade the neutron energy nor effectively remove neutrons from the beam. Multiple scattering in the sample can alter the effective flux as calculated above but this effect is not expected to change the resultant flux by more than 1% for the scattering samples used here. The scattered neutrons are also corrected for attenuation in the scattering sample and for the detection efficiency of the neutron detector.

### 2.3 Results

Neutron time-of-flight spectra obtained during the present experiment are shown in Figs. 6 through 13. Vertical arrows on the figures show the position of neutrons scattered to specific excited levels in the nucleus. Backgrounds have been subtracted from all of the figures.

The elastic scattering angular distribution curves are shown in Fig. 14 through 25. Relative errors on the points due to statistics and background stripping are of the order of 3% near the minima and less than 1% elsewhere and lie within the data points shown. The curve shown on each figure is a visual fit to the experimental points and Wick's limit in the forward direction, and is extrapolated in the backward direction from the last experimental point to 180°. The direction of the extrapolation is chosen to conform with similar curves at nearby energies. The curves have not been corrected for multiple scattering which should have the effect of lowering the values in the vicinity of the minima and slightly increasing those at the forward angles.

Tabular values of the experimental elastic measurements are given in Tables 1 through 12. The errors indicated on the differential measurements are assigned the upper limit of the errors estimated from stripping and statistics and do not include an error of 8.2% estimated to be in the normalization to absolute cross sections. The integrated cross sections indicated on the tables

were obtained from graphical integration of the curves. The errors indicated on the integrated cross sections include the 8.2% error in the normalization to absolute cross sections. Also included on each table is the calculated value for Wick's limit and the total cross section used in this calculation.

Inelastic neutron cross sections for prominent discrete peaks such as those in oxygen were obtained over a large angular region. For other elements, where it was necessary to take additional helium measurements to remove backgrounds in the inelastic region, inelastic cross sections were measured at only one or two angles due to the time economies involved. Tabulated values of the inelastic measurements are given in Tables 13 through 25. Where possible the inelastic neutrons have been specified in terms of nuclear excited states. In those cases where the inelastic neutrons appeared as a continuum the cross sections are reported in energy bins and the corresponding range of excitation is also given.

The errors shown on the differential cross sections are our estimates of the stripping and statistical errors only. The inelastic measurements indicate isotropy of the neutron distribution so that an integrated inelastic value is obtained by multiplying the differential value by  $4\pi$ . The errors on the integrated cross sections shown in Tables 13 through 25 include the 8.2% absolute normalization error.

## Nitrogen

The time-of-flight spectra obtained from nitrogen at  $E_n = 9.0$  and  $E_n = 11.0$  MeV are shown in Figures 6 and 7. The scattering sample was liquid nitrogen contained in a double walled cylindrical cryostat of LASL design<sup>†</sup>. The cryostat consisted of an inner stainless steel cylinder, 2.679 cm in diameter and 4.165 cm long (volume =  $23.49 \text{ cm}^3$ ), separated from an outer stainless steel jacket by a 0.381 cm thick vacuum gap. The inner cylinder walls were 0.0076 cm thick and the outer walls were 0.0101 cm thick. An empty stainless steel container identical in design to the cryostat was used to obtain the background runs.

The positions of the known energy levels in nitrogen are indicated by the arrows on Figures 6 and 7. The resolution of the detector system coupled with the weak excitation of the level fails to show any evidence of a peak corresponding to excitation of the first level at 2.31 MeV. Neutron groups corresponding to other levels in nitrogen are not too well resolved except for those going to the second and ninth levels at 3.945 MeV and at 7.028 MeV as seen in Figure 7.

The cross sections for elastic scattering are listed in Tables 1 and 2. A small contribution from the excitation of the 2.313 MeV level which may have been included in the integration of the elastic peak has been neglected since it is reported<sup>6,7</sup>

<sup>†</sup>We are indebted to E. Kerr of CMF-9 at LASL for use of the cryostat and for providing the container dimensions and pressure density curves used in the calculations.

to be less than a few mb/sr. Errors indicated on the differential measurements are the maximum estimates of the stripping and statistical errors. The integrated cross sections obtained by graphical integration (and which include the absolute normalization error of 8.2%) have values considerably larger than those reported recently.<sup>7</sup>

The inelastic cross sections are listed in Tables 13 and 14. The tables indicate appreciable excitation of high energy levels in nitrogen. The errors in the differential cross sections are stripping and statistical errors only, while the integrated cross section error includes the absolute normalization error.

### Oxygen

Time-of-flight spectra for oxygen at  $E_n = 9.0$  and  $E_n = 11.0$  MeV are shown in Figures 8 and 9. The scattering sample consisted of a thin walled (.05 cm) brass cylinder, 4.35 cm long with an ID of 1.905 cm, which held approximately 2/3 mole of water. Backgrounds were obtained with an empty brass cylinder of the same dimensions. A prominent peak from n,p scattering in the water is observed in both spectra and other peaks seen in the spectra correspond to the indicated energy levels in oxygen.

Elastic scattering cross sections are listed in Tables 3 and 4 and the errors shown are the same as those described for nitrogen. Integrated cross sections in the tables have values somewhat smaller than those reported in the literature.<sup>8,9</sup>

We were able to measure the inelastic scattering to the doublet levels near 6.1 MeV at angles between  $30^\circ$  and  $125^\circ$  at  $E_n = 9.0$  and 11.0 MeV, and to the doublet levels near 7 MeV at  $E_n = 11.0$  MeV. The results, with the relative errors listed in Tables 15 through 17, indicate that the distributions are essentially isotropic. The cross sections for scattering to the 6.1 MeV doublet appear considerably larger at  $E_n = 9.0$  MeV than those obtained from gamma-ray data,<sup>10,11</sup> but are in reasonable agreement at  $E_n = 11.0$  MeV. The values for scattering to the 7 MeV doublet are also larger than the corresponding gamma-ray data. No clear evidence for scattering to the 8.86 MeV level was seen in the spectra but this was expected since the neutrons scattered to this level from the incident 11 MeV beam would have energies close to the neutron bias level on the detector.

#### Aluminum

The time-of-flight spectra for aluminum at  $E_n = 9.0$  MeV is shown in Figure 10. The scattering sample used consisted of a hollow cylinder 2.40 cm O.D., 1.60 cm I.D. and 4.00 cm long. The resolution of the detector was insufficient to resolve the neutrons scattered to the first two levels from the elastic peak. Although the energy levels in aluminum are generally numerous and fairly evenly spaced there appears to be preferential scattering to certain groups of levels as indicated in Figure 10. The three peaks to the left of the elastic peak are characteristic of all

measurements made both at 9 and 11 MeV.

The elastic scattering cross section plots are shown on Figures 18 and 19 and tabular values are listed in Tables 5 and 6. A contribution from the 0.843 and 1.013 MeV levels of 4 mb/sr has been subtracted from each measured point at  $E_n = 9$  MeV and a contribution of 3 mb/sr has been subtracted from each measured point at  $E_n = 11$  MeV. The errors shown in the tables are the same as those indicated in the nitrogen section. Inelastic cross section values are listed in Tables 18 and 19. The 9 MeV integrated elastic cross section listed in Table 5 is in good agreement with the Oak Ridge results<sup>12</sup> at 8.56 MeV.

#### Silicon

Figure 11 shows the time-of-flight spectrum from silicon at  $E_n = 9.0$  MeV. The scattering sample was a solid cylinder 2.58 cm in diameter and 3.97 cm long. The first excited level at 1.779 is clearly separated from the elastic peak. Positions of other excited levels are indicated by the vertical arrows. The elastic scattering cross sections are plotted on Figures 20 and 21 and the tabulated values are listed in Tables 7 and 8. The inelastic cross sections are listed in Tables 20 and 21. The integrated elastic scattering cross section at 9 MeV shown in Table 7 is in excellent agreement with the 8.56 MeV results from Oak Ridge.<sup>13</sup>

### Calcium

A spectrum obtained from calcium at  $E_n = 11.0$  MeV is shown in Figure 12. The scattering sample was a solid cylinder 2.35 cm in diameter and 4.50 cm long. The first excited level in  $^{40}\text{Ca}$  at 3.35 MeV while well separated from the elastic peak is not resolved from other close lying levels. The spectra exhibit a continuum above about 4.5 MeV. Elastic scattering cross sections are shown in Figures 22 and 23 and tabular values are listed in Tables 9 and 10.

The inelastic cross sections are listed in Tables 22 and 23. The integrated elastic cross section in Table 9 is in good agreement with recent Oak Ridge results<sup>14</sup> at 8.5 MeV, and the inelastic cross sections to the first four levels listed in Table 22 are in close agreement as well.

### Iron

The time-of-flight spectrum from iron at  $E_n = 9.0$  MeV is shown in Figure 13. The scattering sample was a hollow cylinder 2.20 cm O.D. 1.60 cm I.D. and 4.00 cm long. No levels are clearly separated and the results in the inelastic region have been analyzed as a continuum. The measured elastic angular distributions are plotted in Figures 24 and 25 and numerical values are listed in Tables 11 and 12. The 9.0 MeV results of Table 11 have had 6 mb/sr subtracted from each measured point to

account for neutrons scattered to the 0.845 MeV level. This value was obtained by stripping the peak at  $120^\circ$  where the elastic scattering is comparable to the inelastic scattering to the 0.845 level. The 11 MeV results of Table 12 have also had  $6 \text{ mb} / \text{sr}$  subtracted from each point as determined from a similar stripping procedure. Errors indicated in the tables have been described in the section on nitrogen. The 9 MeV integrated elastic cross section listed on Table 11 agrees within the error limits with the Oak Ridge results<sup>15</sup> at 8.56 MeV. Inelastic scattering values are listed in Tables 24 and 25.

### 3. GAMMA RAY MEASUREMENTS

#### 3.1 Data Acquisition

The experimental geometry and procedures used to acquire the gamma-ray data were the same as those described in the previous report<sup>1</sup> except that only the NaI(Tl) center detector was used in the present work.

Basically, the gamma-ray data were obtained with a large two-crystal anticoincidence spectrometer (whose operation has been described elsewhere),<sup>16,17</sup> operated in conjunction with conventional pulsed beam time-of-flight techniques to reduce neutron and time-random backgrounds. The anticoincidence operation of the spectrometer greatly reduces the Compton scattering components in the gamma-ray energy spectra thus considerably simplifying the analysis of complex spectra. Neutron backgrounds caused by neutrons scattering into the detector are reduced by gating the linear spectrum with only that portion of the time-of-flight spectrum corresponding to prompt gamma-ray events. The anticoincidence feature, whose main purpose is to reduce the Compton scattering, is also very effective in reducing time-random neutron and gamma-ray backgrounds.

A diagram of the gamma-ray spectrometer with a NaI(Tl) center detector in position is shown in Fig. 26. The scattering samples were the same as those used for the neutron work, and the gas target to sample distance used was 8 cm. The sample to NaI(Tl)

center detector was maintained at 130 cm and the detector angle was maintained at 55° throughout the experiment.

The efficiency of the gamma-ray spectrometer as a function of gamma ray energy was determined with calibrated radioisotopic sources up to an energy of 3 MeV and by indirect techniques above this energy. Fig. 27 shows the detector efficiency as a function of gamma ray energy. The two calibration points at 4.43 MeV were determined from the  $^{15}\text{N}(\text{p},\alpha\gamma)^{12}\text{C}$  reaction and from the n/γ ratio of a calibrated AmBe source. The 11.7 MeV data point was obtained from the  $^{11}\text{B}(\text{p},\gamma)^{12}\text{C}$  reaction and the data point at 10.8 MeV was obtained from the  $^{14}\text{N}(\text{n},\gamma)^{15}\text{N}$  reaction.<sup>18</sup> The last measurement was obtained with a reactor\*

Production of neutrons and methods used for determining the neutron flux were the same as those described in Section 2.1. Data runs consisted of both sample-in and sample-out runs and for the 11 MeV work, additional sample-in, sample-out runs were made with the target cell filled with helium.

Two gated linear spectra were accumulated simultaneously, the first spectrum corresponding to those events falling within the prompt gamma-ray gate on the time-of-flight spectrum, the second corresponding to those events falling within an equivalent gate set on the flat, or time-random background portion of the spectrum. The spectra were stored in the SDS computer along with

\* This measurement was made at the Omega West reactor site at LASL. The authors would like to acknowledge the use of this site and to thank Dr. E. T. Jurney for performing this measurement.

the difference spectra of the two. Adjustment of gate widths and proper operation of the subtraction process was checked with a radioactive source. The data were recorded on magnetic tape and on paper print out for later analysis. Subtraction of the helium gas cell runs from the tritium gas cell runs were made on the IBM-1130 computer at Texas Nuclear.

### 3.2 Data Reduction

The analysis of the gamma-ray data like that for the neutrons begins with subtraction of a properly normalized sample-out run from a sample-in run. The difference spectrum is then stripped by empirical procedures based on monoenergetic line shapes, starting at the high energy end of the spectrum, and removing at each operation the related Compton distribution from the lower portions of the spectrum. The resulting counts are corrected for self-absorption of gamma rays in the scattering sample by the method of Cranberg and Levin,<sup>4</sup> and for the gamma-ray efficiency of the detector. The corrected counts are then converted to gamma-ray production cross sections by conventional means using the effective neutron flux determined as described in Section 2.2. Since the angular dependence of most gamma-ray distributions can be described by the first two terms of an even order Legendre polynomial expansion, integrated cross sections could be obtained by multiplying the present 55° differential cross sections by  $4\pi$ .

It should be noted that the cross sections reported for discrete gamma rays in Tables 26-32 may also contain some contribution from continuum gamma rays. The procedure used is to include all observed counts in the energy bin of interest and to subtract from these counts only the Compton scattering contribution from all of the higher energy bins considered. Under these conditions, if the sum of all Compton contributions considered is less than the apparent continuum on the high energy side of the discrete peak in question, then the cross section for the discrete peak will contain

some continuum. An example of the opposite case occurs in Figure 28 for the 5.10 MeV discrete peak. Here the sum of the Compton contributions is just equal to the continuum to the right of the peak. In this case the 5.10 MeV peak cross section contains no unresolved gamma ray contribution.

### 3.3 Results

Fewer gamma-ray measurements than originally proposed were completed. Difficulties in the form of a very high background appeared the low energy region of the gamma-ray spectrum and made portions of the spectra unuseable in addition to causing considerable loss of time. The origin of the background was not ascertained although it was found to be present in the three different detector systems tried. The background was less intense with the 9 MeV neutrons than with those at 11 MeV. Typical spectra obtained are shown in Figures 28 through 30. The lower part of the spectra were not useable due to the high backgrounds encountered. Tabular values of the cross sections measured are listed in Tables 26 through 32. The errors shown consist of an 8% estimated error in the absolute cross-section normalization with the remainder due to stripping, statistics and difficulties in positioning the time gates. Due to the nature of the background problems encountered in the acquisition of the gamma-ray production data, the results given in Tables 26 through 32 should be considered as preliminary and not for quotation. Additional work will be required to remove the uncertainties associated with these data.

#### Nitrogen

The gamma-ray spectrum of nitrogen, obtained with 11 MeV incident neutrons is shown in Figure 28. In addition to gamma rays from inelastic scattering, others from  $^{11}\text{B}$ ,  $^{13}\text{C}$  and  $^{14}\text{C}$  produced by  $(n,\alpha)$ ,  $(n,d)$  and  $(n,p)$  reactions are observed.

The spectrum is similar to that observed at 14.8 MeV.<sup>19</sup> Difficulties with the nitrogen cryostat were encountered during the run so that it was necessary to use a different scattering sample. The data shown here were taken with a cylinder of  $\text{Be}_3\text{N}_2$ , 3.83 cm in diameter and 5.43 cm long. Prior to the measurement the sample was analyzed at the Omega West reactor site for possible carbon contamination and was found to contain negligible amounts.

Gamma-ray production cross sections are listed in Table 26. The integrated cross section shown in the table is in good agreement with the Oak Ridge results,<sup>20</sup> but gamma ray-production cross sections for individual levels such as the prominent 4.46 and 5.10 MeV peaks in Figure 28 are considerably larger than the Oak Ridge values. Reasonable agreement with the integrated cross section of the GGA group<sup>21</sup> is also found but individual level excitations show considerable differences. The integrated cross section indicated in Table 26 less the contribution from  $^{11}\text{B}$  and  $^{13}\text{C}$  indicated in the table, is in reasonable agreement with the inelastic cross section listed in Table 14 as well.

#### Oxygen

Gamma ray production cross sections for oxygen are listed in Table 27. The large background mentioned interferes with the measurement of the 2.74 MeV gamma ray from the 8.86 MeV level but the remainder of the spectrum appeared satisfactory. The results of the three gamma ray groups, 3.68 and 3.86 MeV from  $^{13}\text{C}$ , 6.13 from  $^{16}\text{O}$  and the 6.92 and 7.12 MeV doublet from

$^{16}\text{O}$  are in excellent agreement with the work of Dickens and Perey.<sup>10</sup> Reasonable agreement with the work of Orphan et al<sup>11</sup> is also shown except for the 6.92 and 7.12 MeV doublet where the present values are almost a factor of two larger than the latter authors. The gamma-ray data for the 6.13 MeV level are in reasonable agreement with the neutron inelastic scattering values of Table 16 but the gamma-ray cross sections for the 6.92 and 7.12 MeV doublet do not agree with the neutron inelastic data in Table 17.

#### Aluminum

The gamma-ray spectrum obtained from aluminum at  $E_n = 9.0$  MeV is shown in Figure 29. Gamma ray peaks corresponding to the first two excited levels are lost due to the high background mentioned earlier. The peaks shown on the figure correspond to a transition from the 2.73 MeV level to the 1.01 MeV level, and three ground state transitions from the 3rd, 5th, and 6th excited levels.

Cross sections for gamma-ray production were obtained at both  $E_n = 9.0$  MeV and  $E_n = 11.0$  MeV and the values are listed in Tables 28 and 29. Comparison of the gamma-ray cross sections with the inelastic cross sections listed in Tables 18 and 19 are difficult without some prior knowledge of the gamma ray multiplicity. The gamma ray cross sections of Table 28 for the 1.72, 2.209 and 3.00 MeV discrete gamma rays however are in good agreement with the 7.5 MeV neutron results from the LASL group.<sup>22</sup>

### Silicon

No gamma-ray measurements were made on silicon in this experiment. These measurements were made earlier and are found in the previous report.<sup>1</sup>

### Calcium

The gamma ray spectrum obtained for calcium at  $E_n = 9.0$  MeV is shown in Figure 30. Two gamma peaks from  $^{37}\text{Ar}$  produced by the  $n,\alpha$  reaction are seen in the spectrum. Cross section values are listed in Tables 30 and 31. Again it is difficult to make comparisons of the gamma-ray yield with the inelastic cross sections. Previous work<sup>23</sup> at  $E_n = 5$  MeV gave a gamma-ray cross section of 14.7 mb/sr for the combined 3.73 and 3.90 MeV gamma rays which makes the values obtained here appear reasonable.

### Iron

Gamma-ray production cross sections obtained for iron at  $E_n = 9.0$  MeV are listed in Table 32. Gamma ray peaks corresponding to 1.03, 1.24, 1.81, 2.11, and 2.65 were observed in the spectrum but since these were not clearly separated from the continuum the whole spectrum was analyzed in energy bins as seen in Table 23. A comparison of the integrated cross section of Table 32 with the integrated inelastic values in Table 24 seem to indicate a gamma ray multiplicity of 2 for iron. This compares

with an evaluated multiplicity<sup>24</sup> of 2.7 for 9 MeV neutrons.

Comparison of the cross sections of Table 32 for  $1 \leq E_{\gamma} \leq 4$  MeV with the results of Dickens and Perey<sup>25</sup> at  $E_n = 9$  MeV over this same energy region indicates agreement within the errors quoted.

#### 4. DISCUSSION

The results presented here represent measurements actually made during the 14 month period January 1970 to March 1971 at Los Alamos Scientific Laboratory. While considerable improvement may be desirable, the results represent a reasonably successful use of the funds allocated and a reasonable achievement of the goals set forth at the onset of the work.

The problems encountered in the form of neutron and gamma-ray backgrounds which have been discussed in previous sections have not prevented the acquisition of data but did make it more difficult. The data acquired are not always susceptible to comparison with the work of others but where this is possible reasonable differences or similarities are generally observed.

It is desirable that additional work in this energy region should be preceded by a fairly comprehensive study of the neutron producing target problems. Specifically the secondary neutrons produced by the target should be further reduced, perhaps by means of different beam stops, and the source of the high intensity gamma-ray background needs to be investigated and eliminated. Finally, measurements should be made at least at one angle with a longer flight path and improved resolution to separate the low lying inelastic levels such as in aluminum and iron.

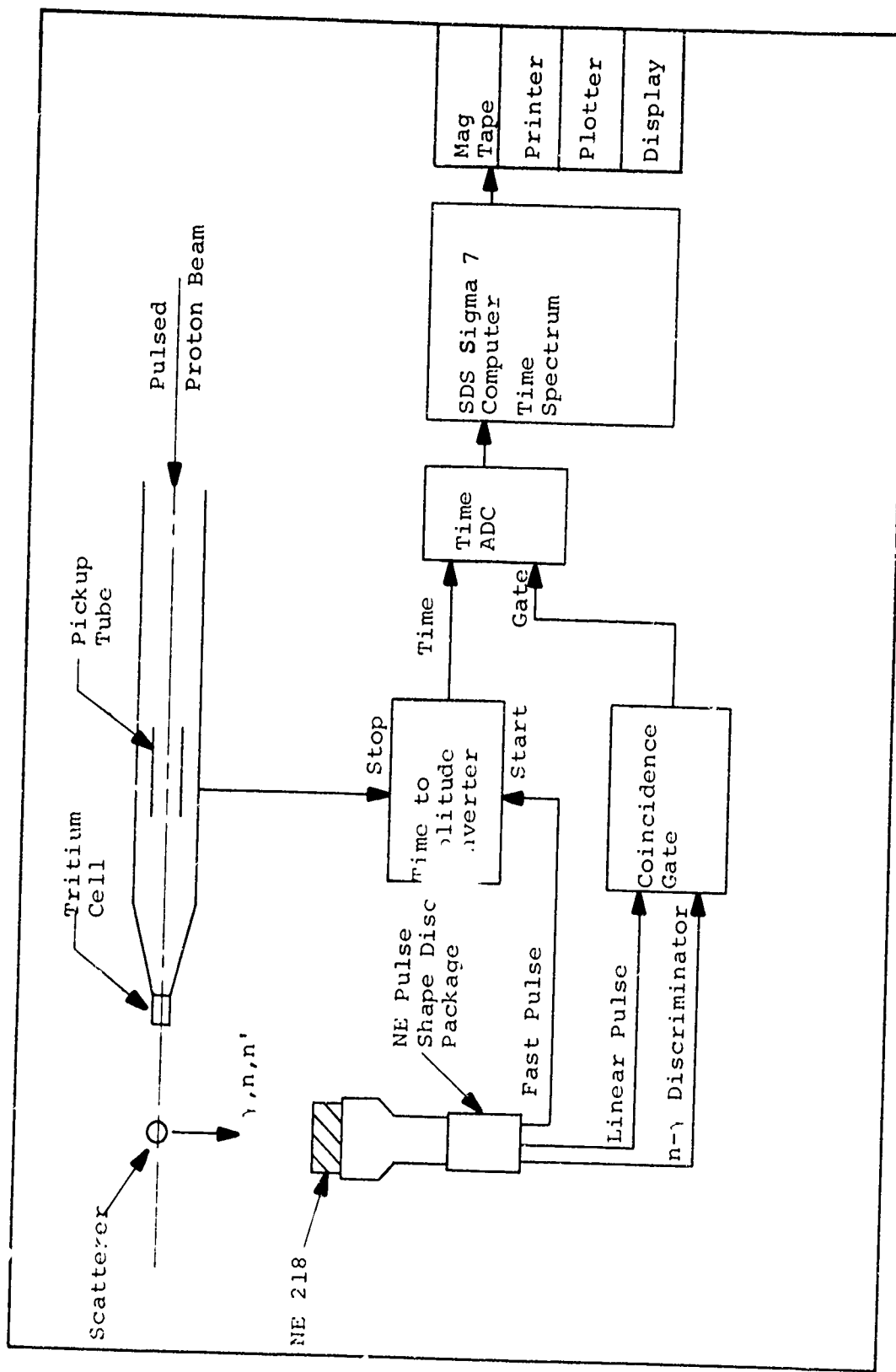


Figure 1. Basic data acquisition system for neutron cross section work at LASL.

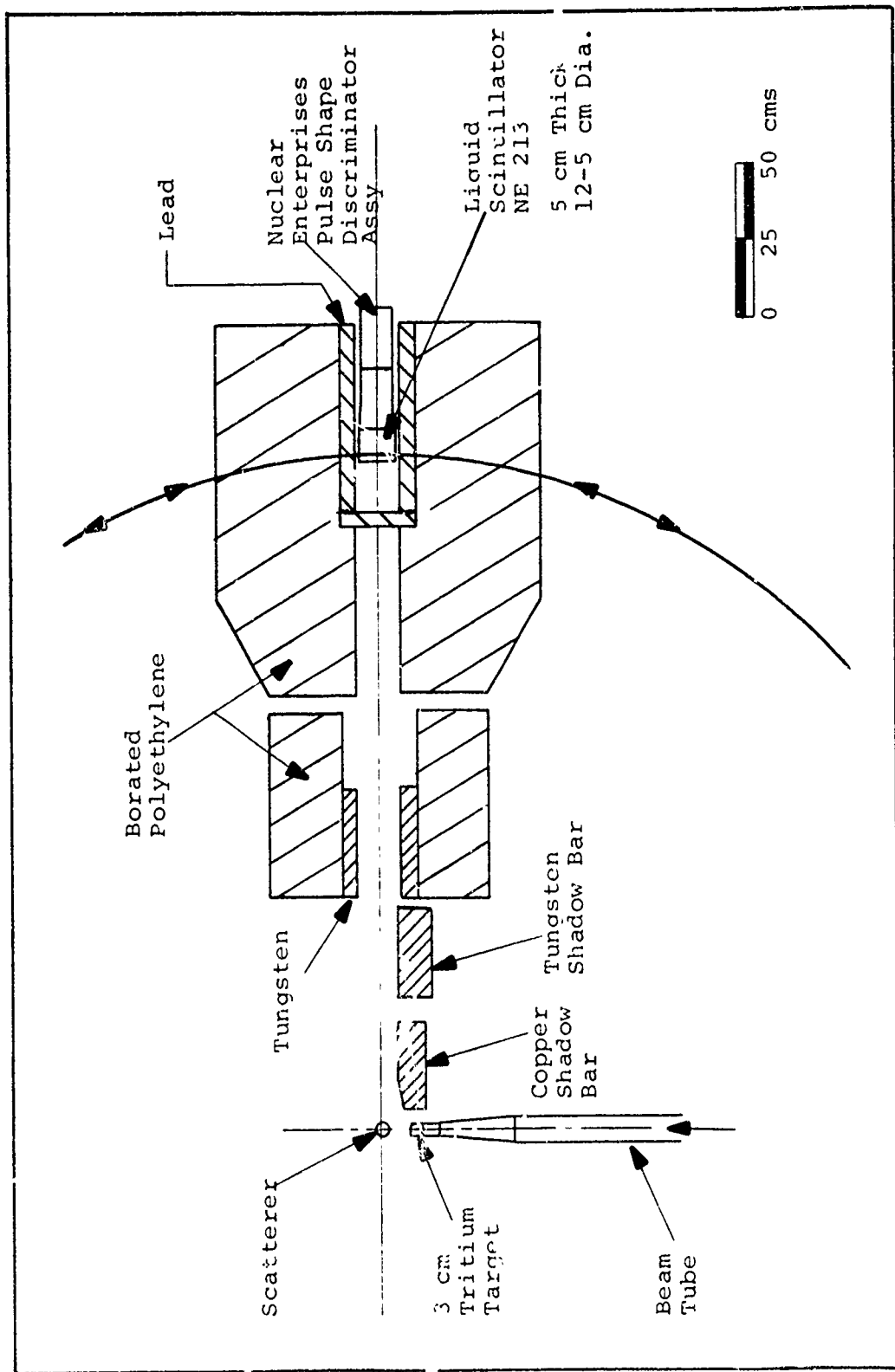


Figure 2. Shielding geometry for neutron cross section work at LASL.

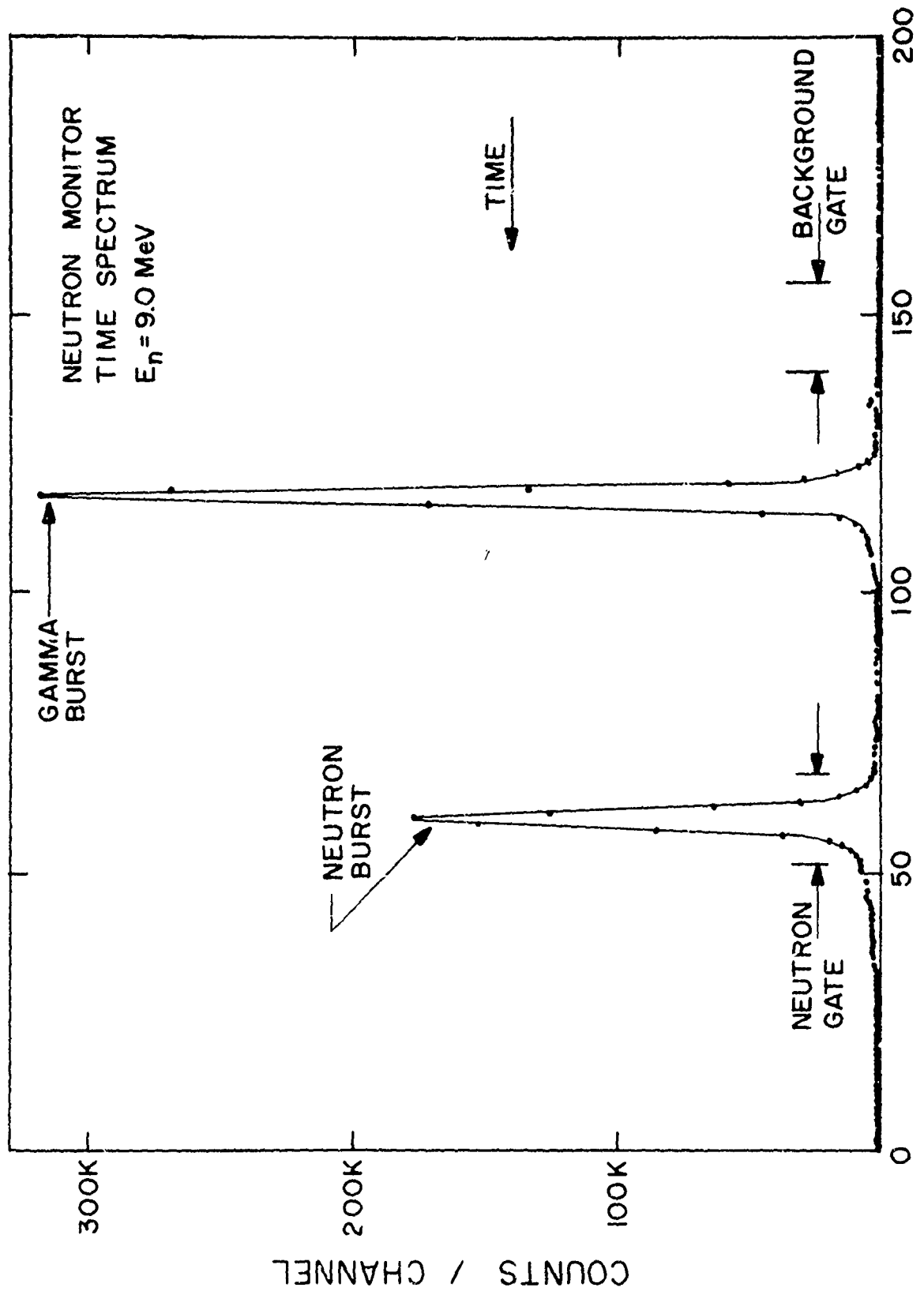


Figure 3. "time-of-flight spectrum from the neutron monitor.

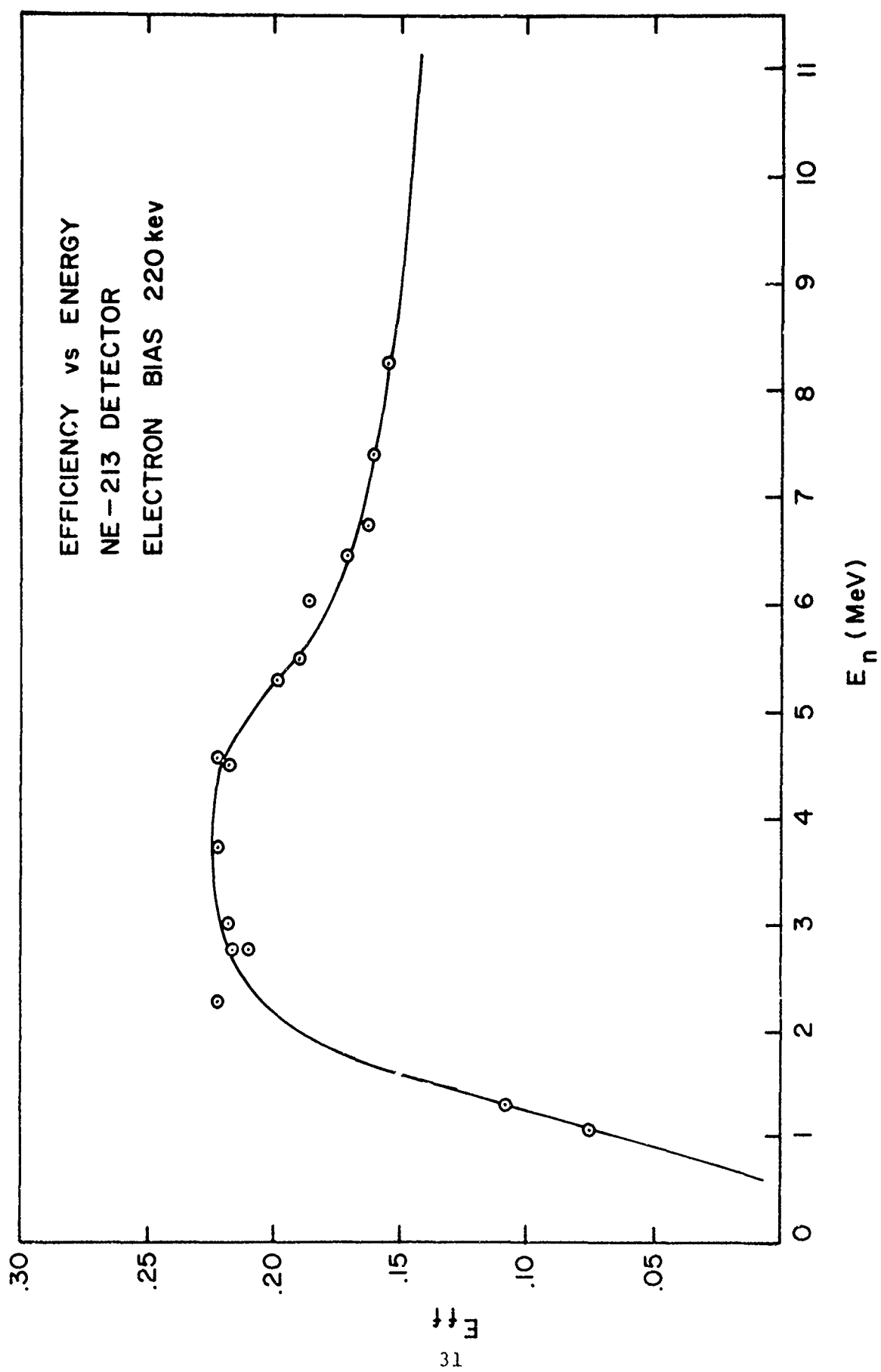


Fig. 4. Efficiency of the NE-213 Neutron Detector

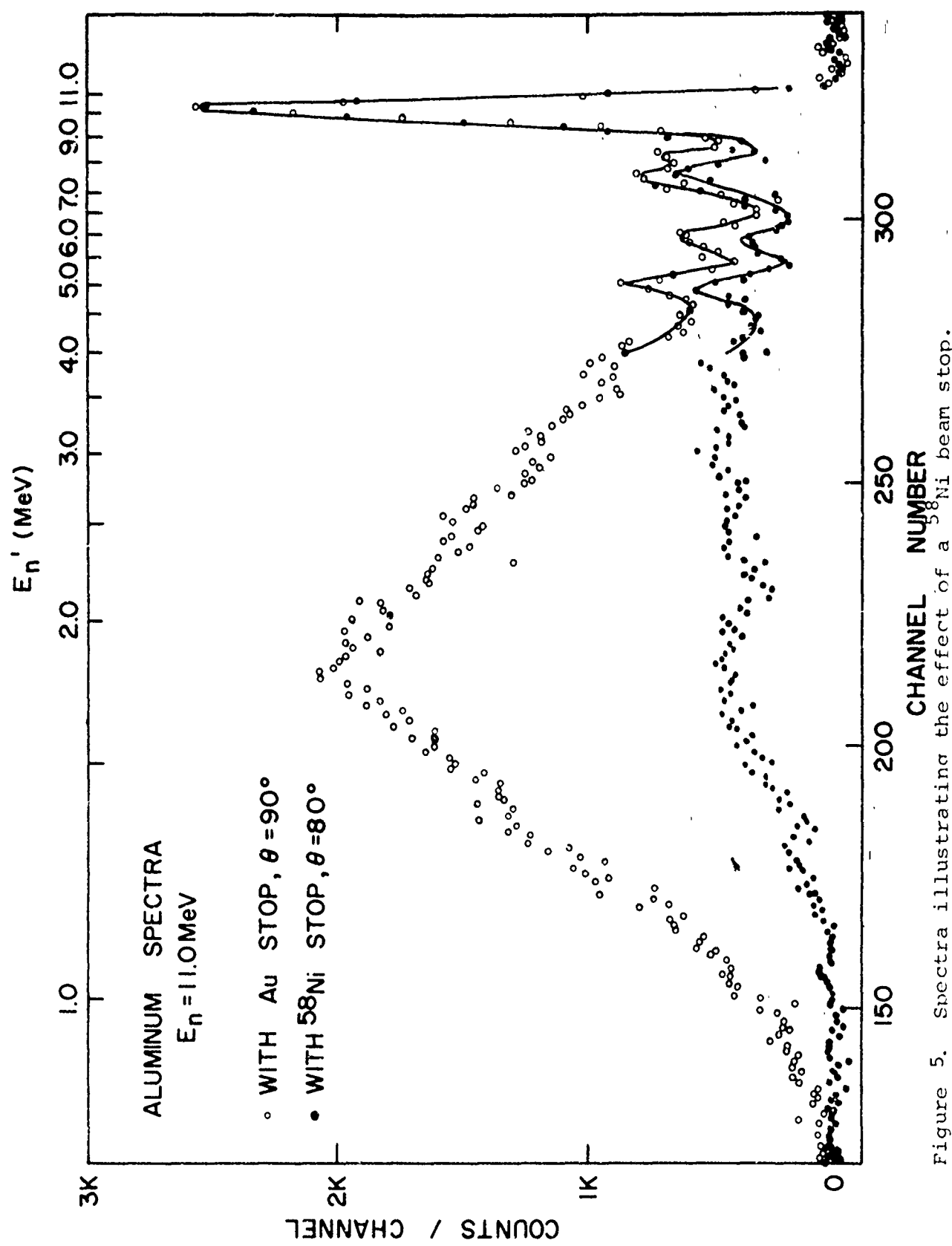


Figure 5. Spectra illustrating the effect of a  $^{58}\text{Ni}$  beam stop.

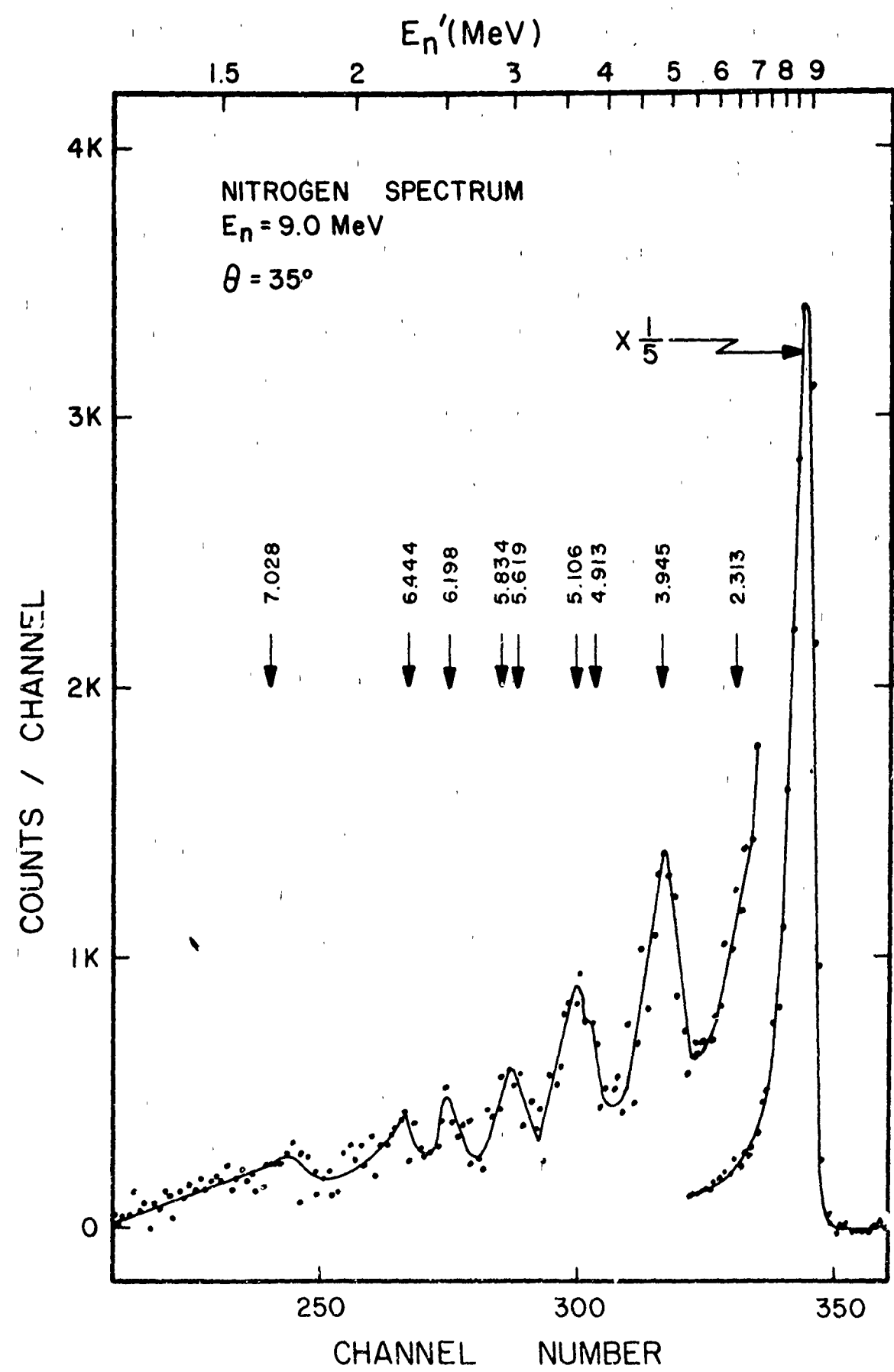


Figure 6. Nitrogen time-of-flight spectrum at  $E_n = 9.0 \text{ MeV}$ .

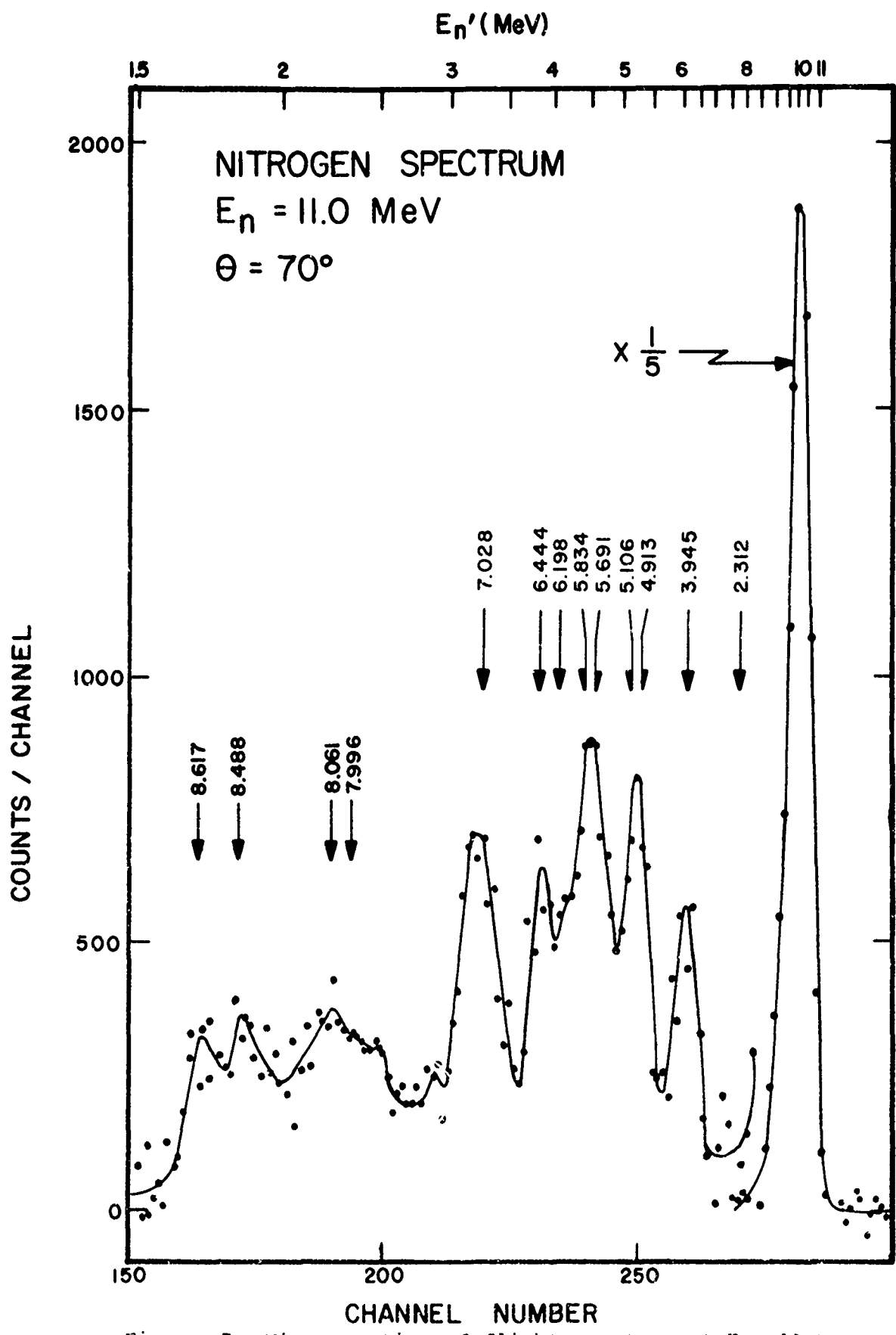


Figure 7. Nitrogen time-of-flight spectrum at  $E_n = 11 \text{ MeV}$ .

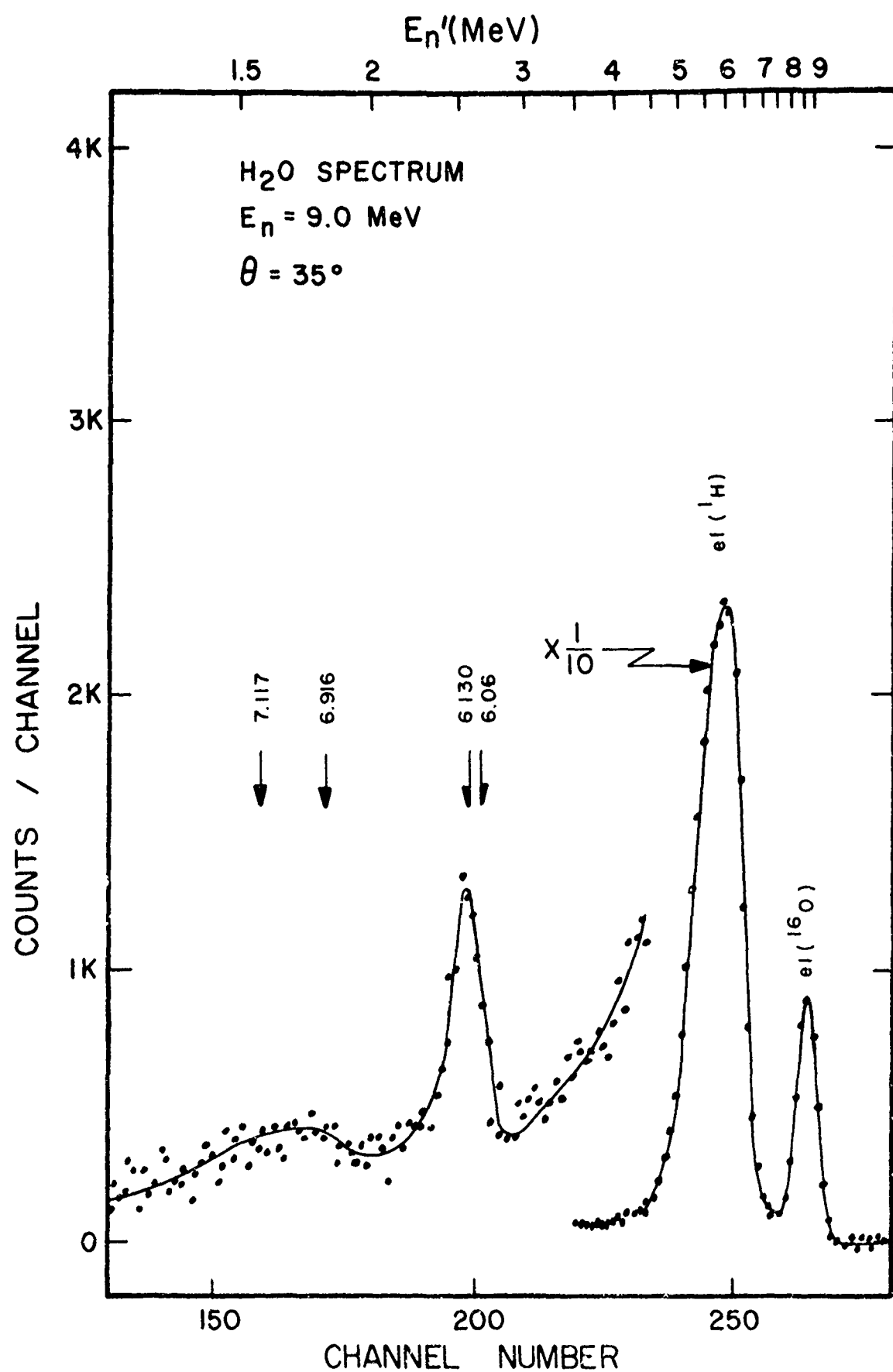


Figure 8. Oxygen time-of-flight spectrum at  $E_n = 9.0 \text{ MeV}$ .

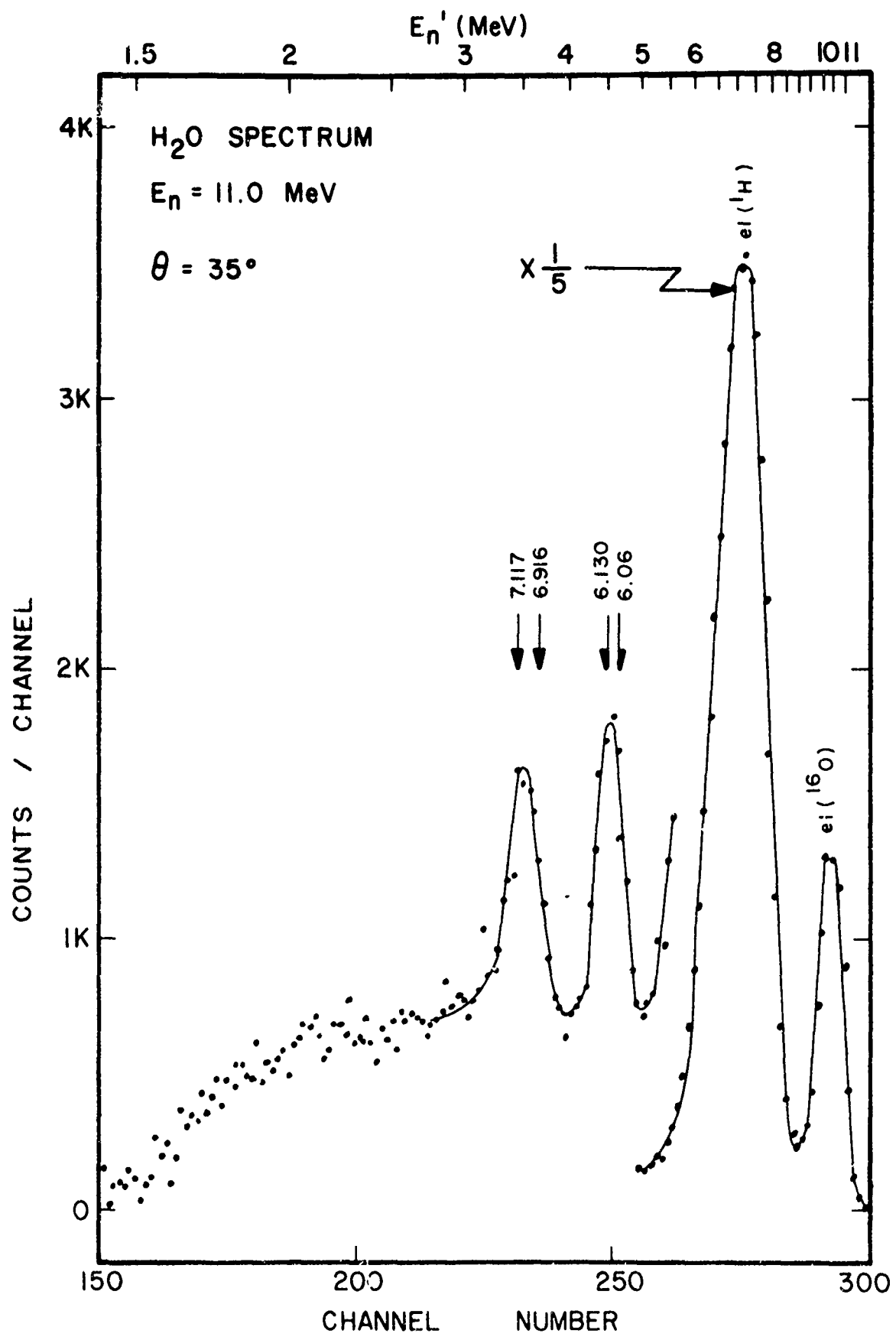


Figure 9. Oxygen time-of-flight spectrum at  $E_n = 11.0$  MeV.

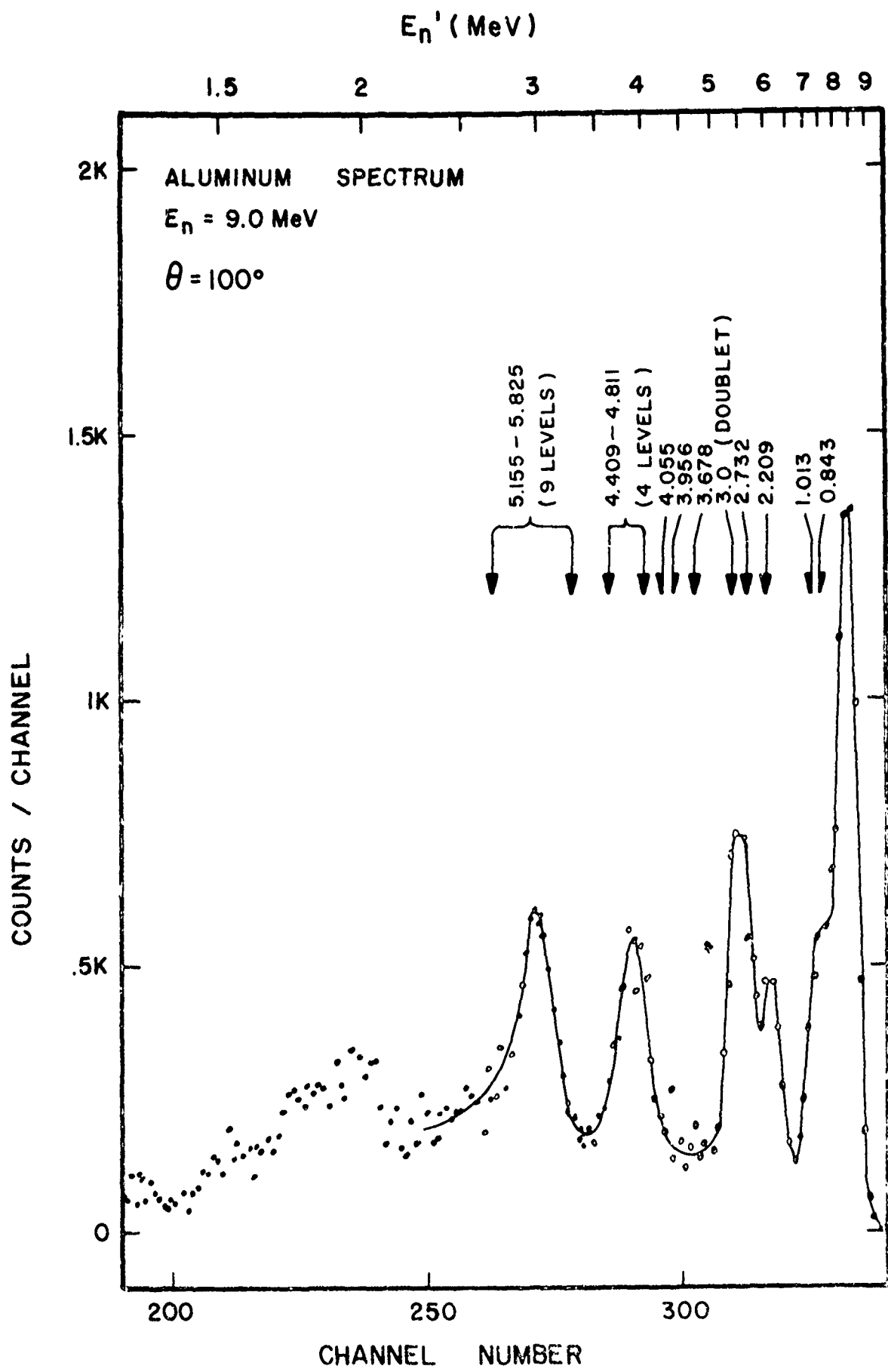


Figure 10. Aluminum time-of-flight spectrum at  $E_n = 9.0 \text{ MeV}$ .

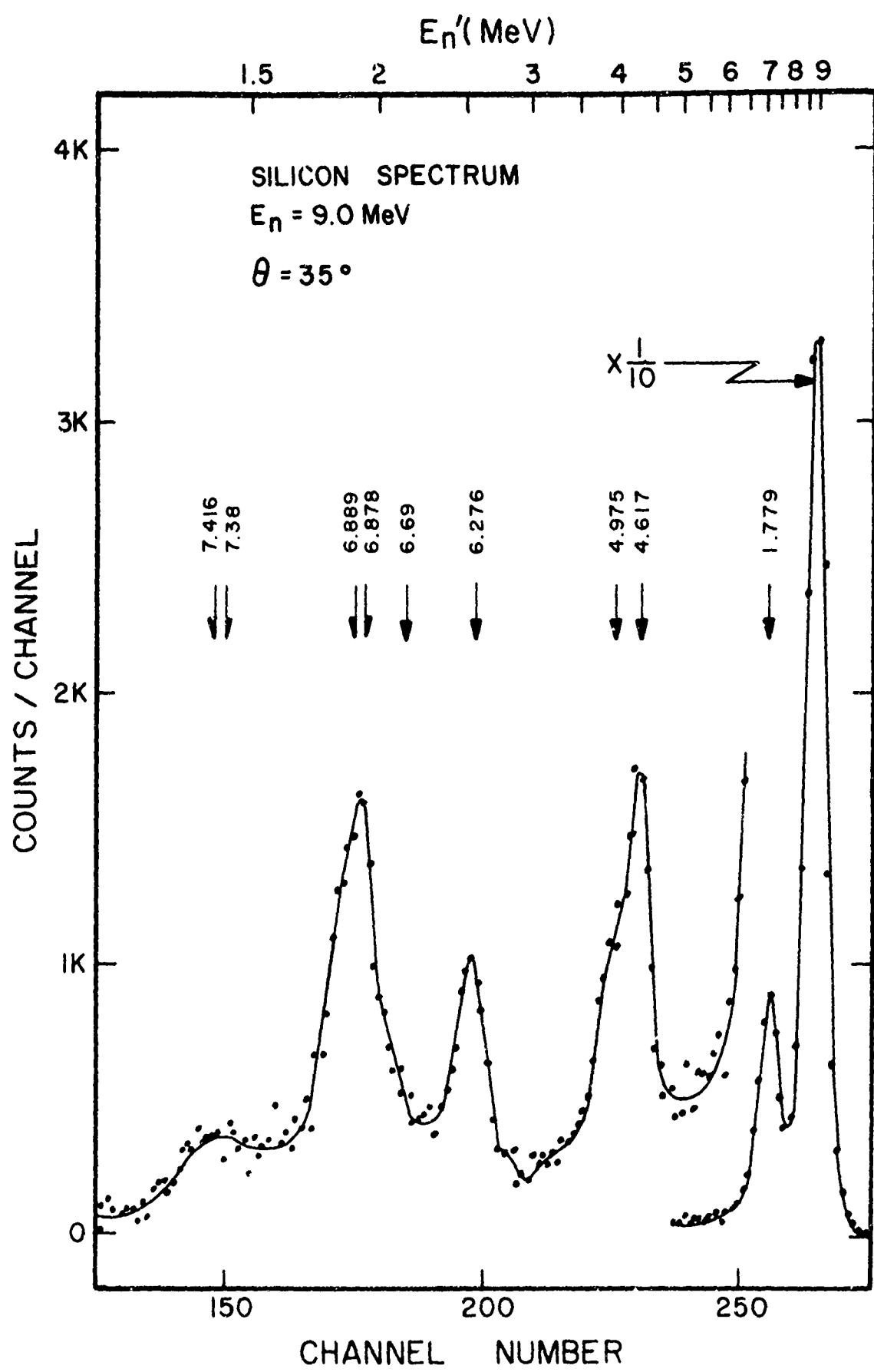


Figure 11. Silicon time-of-flight spectrum at  $E_n = 9.0 \text{ MeV}$ .

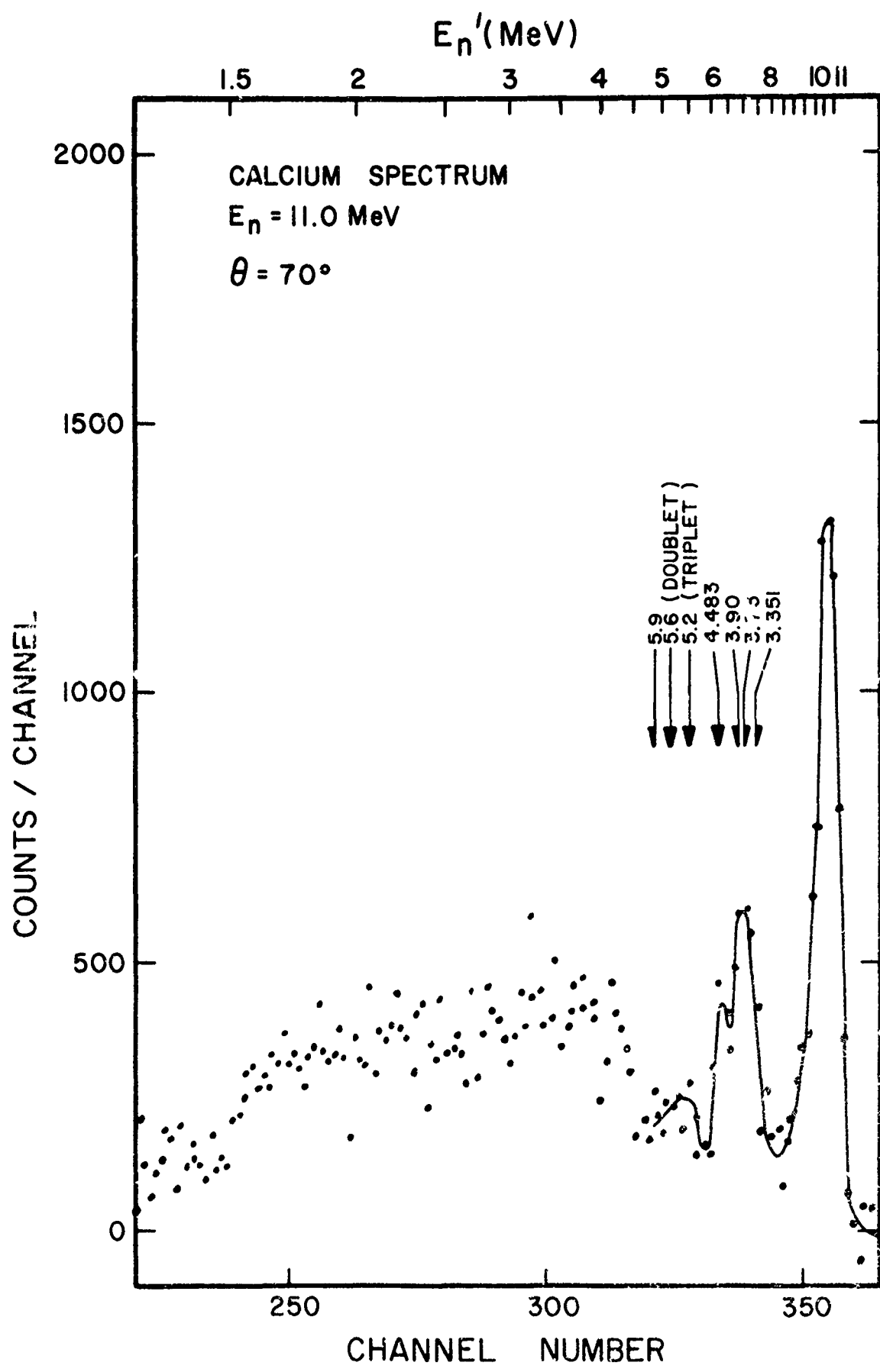


Figure 12. Calcium time-of-flight spectrum at  $E_n = 11.0 \text{ MeV}$ .

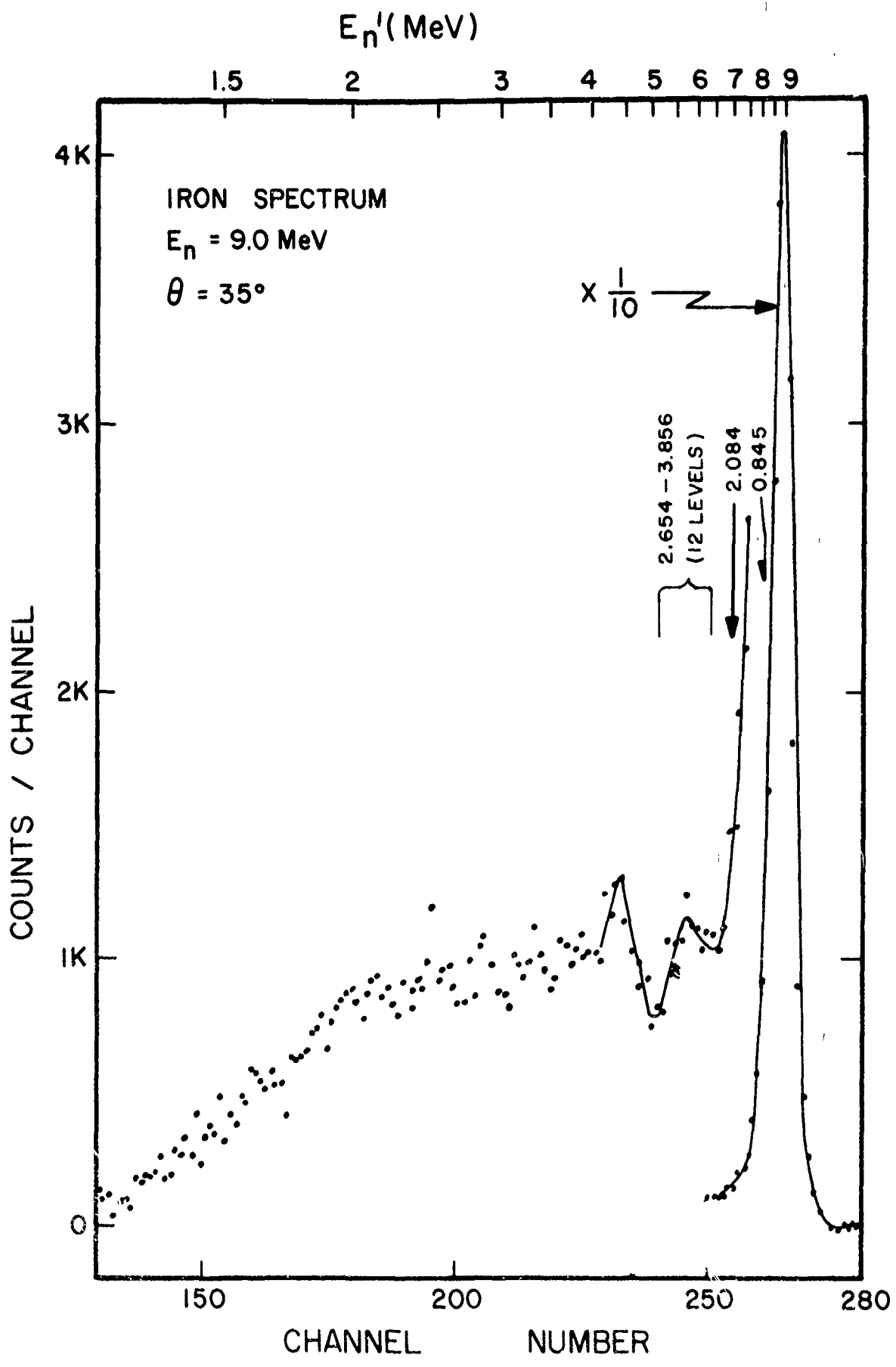


Figure 13. Iron time-of-flight spectrum at  $E_n = 9.0 \text{ MeV}$ .

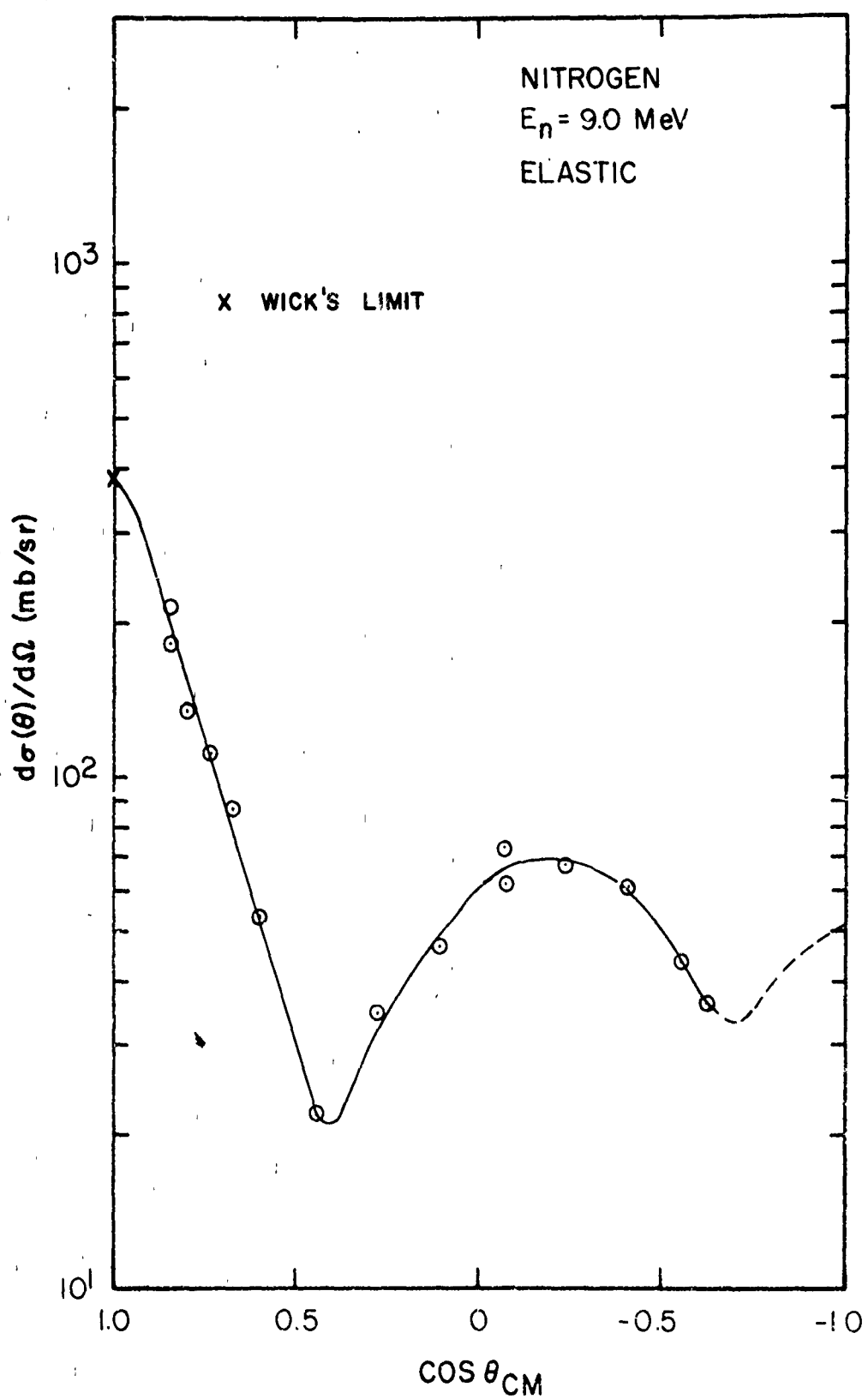


Figure 14. Nitrogen elastic scattering at  $E_n = 9.0$  MeV.

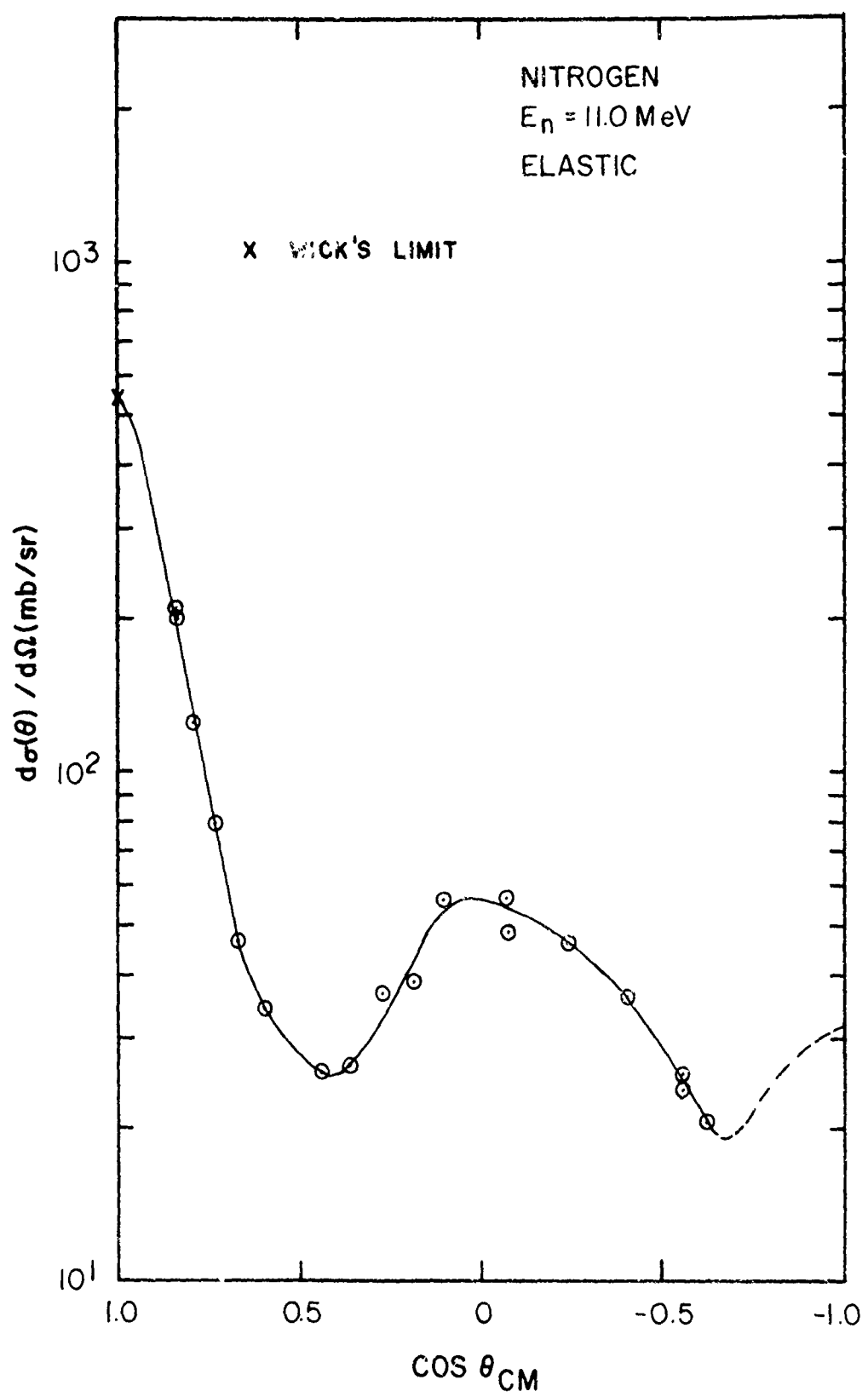


Figure 15. Nitrogen elastic scattering at  $E_n = 11.0 \text{ MeV}$ .

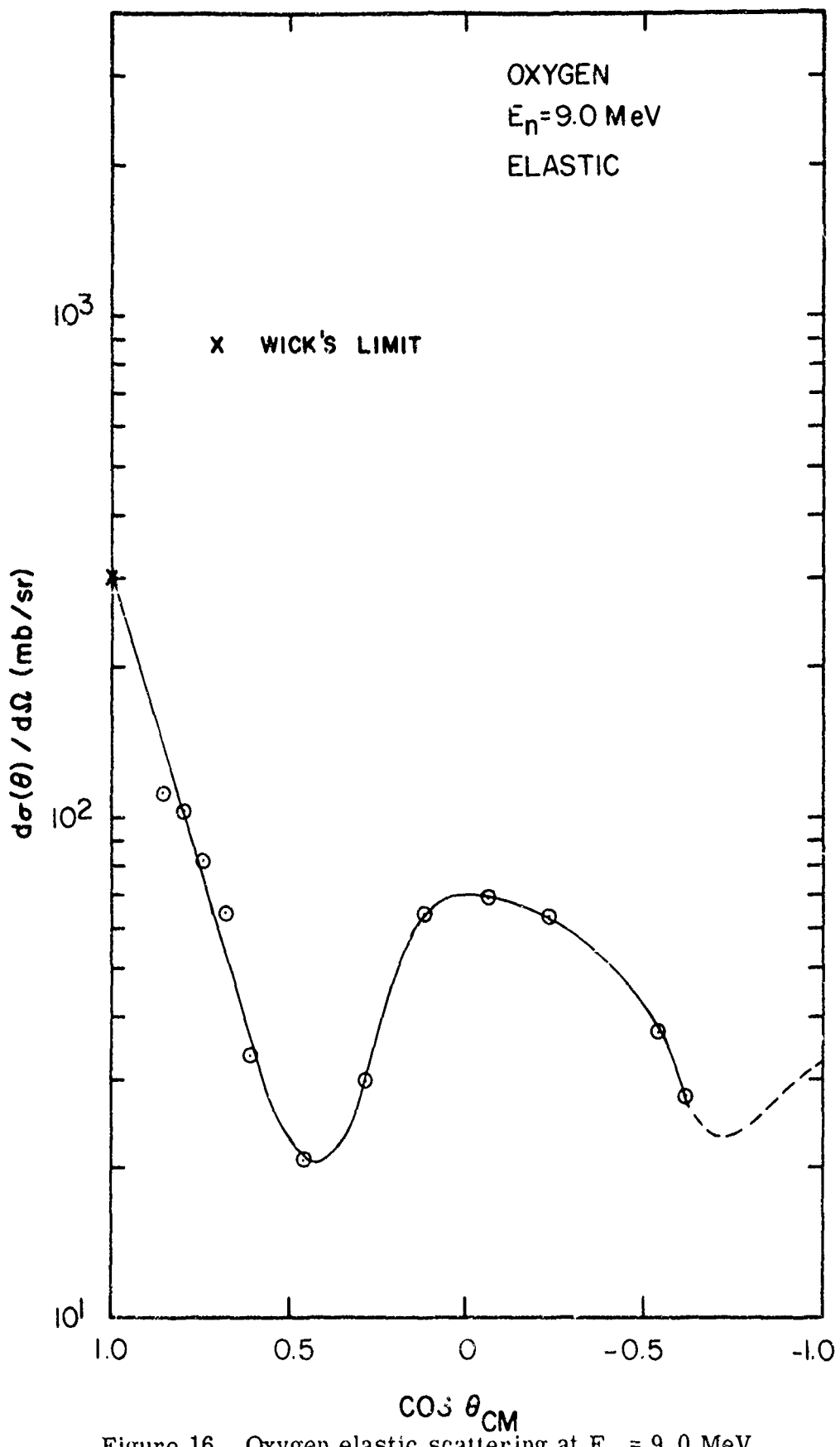


Figure 16. Oxygen elastic scattering at  $E_n = 9.0$  MeV.

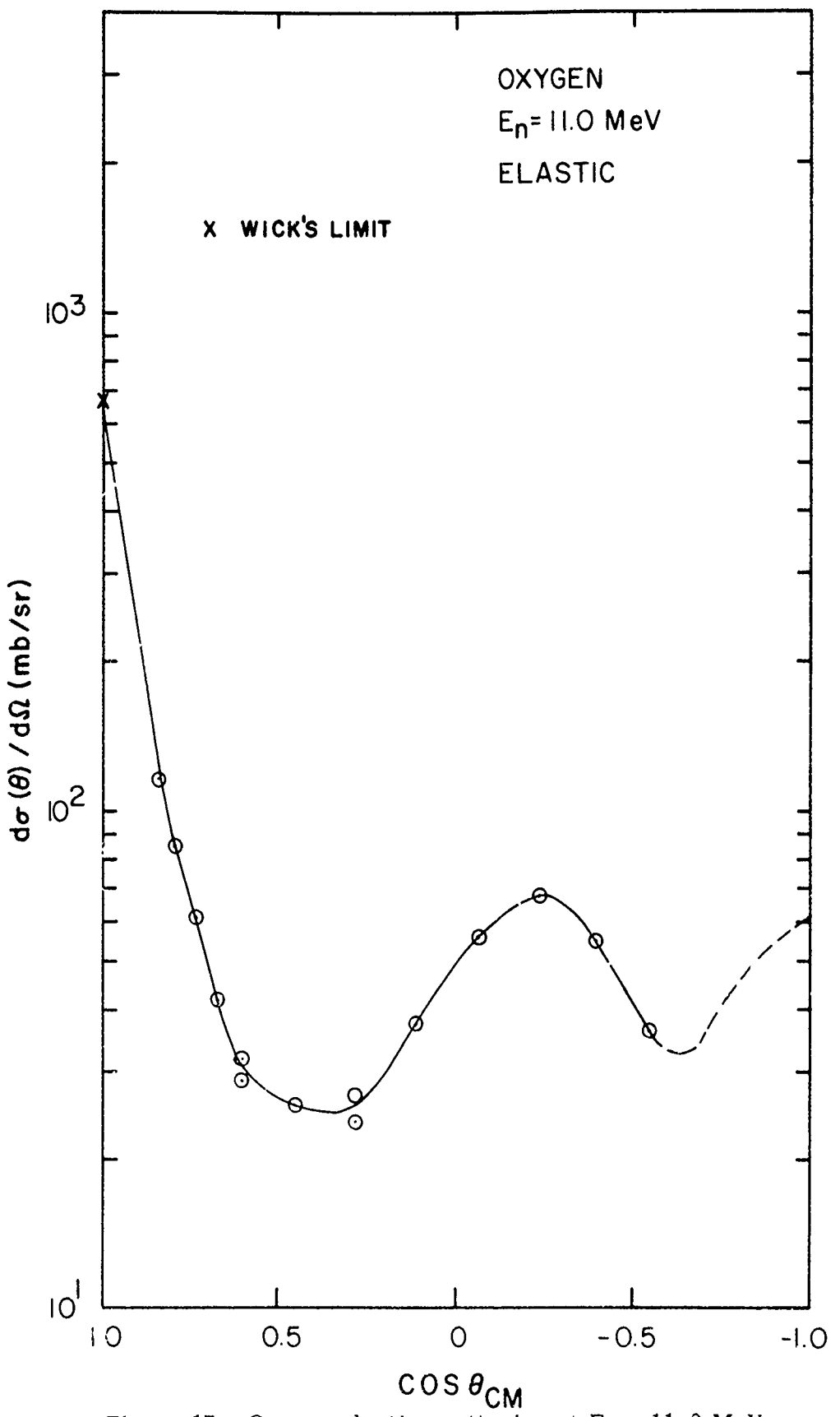


Figure 17. Oxygen elastic scattering at  $E_n = 11.0$  MeV.

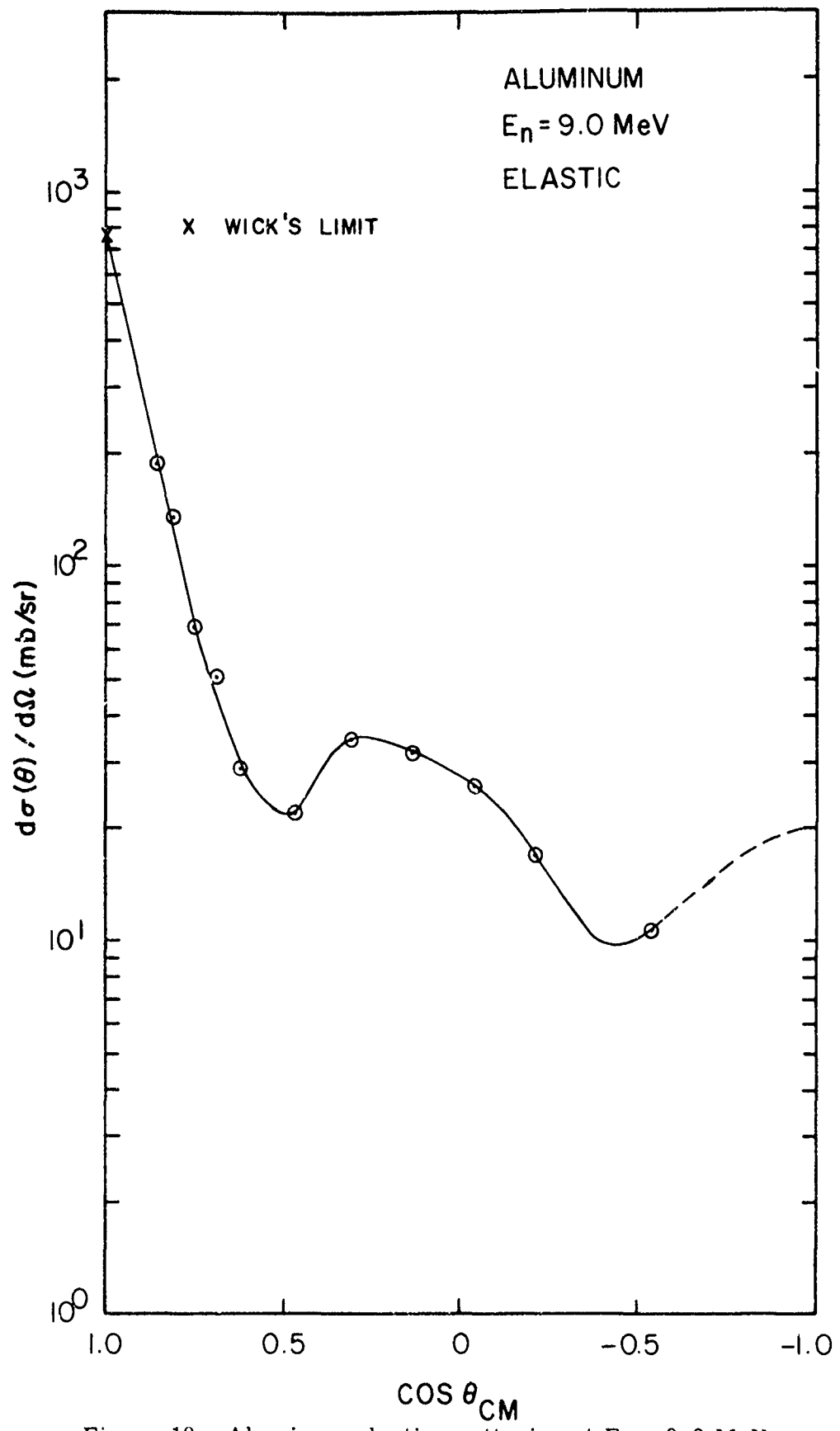


Figure 18. Aluminum elastic scattering at  $E_n = 9.0$  MeV.

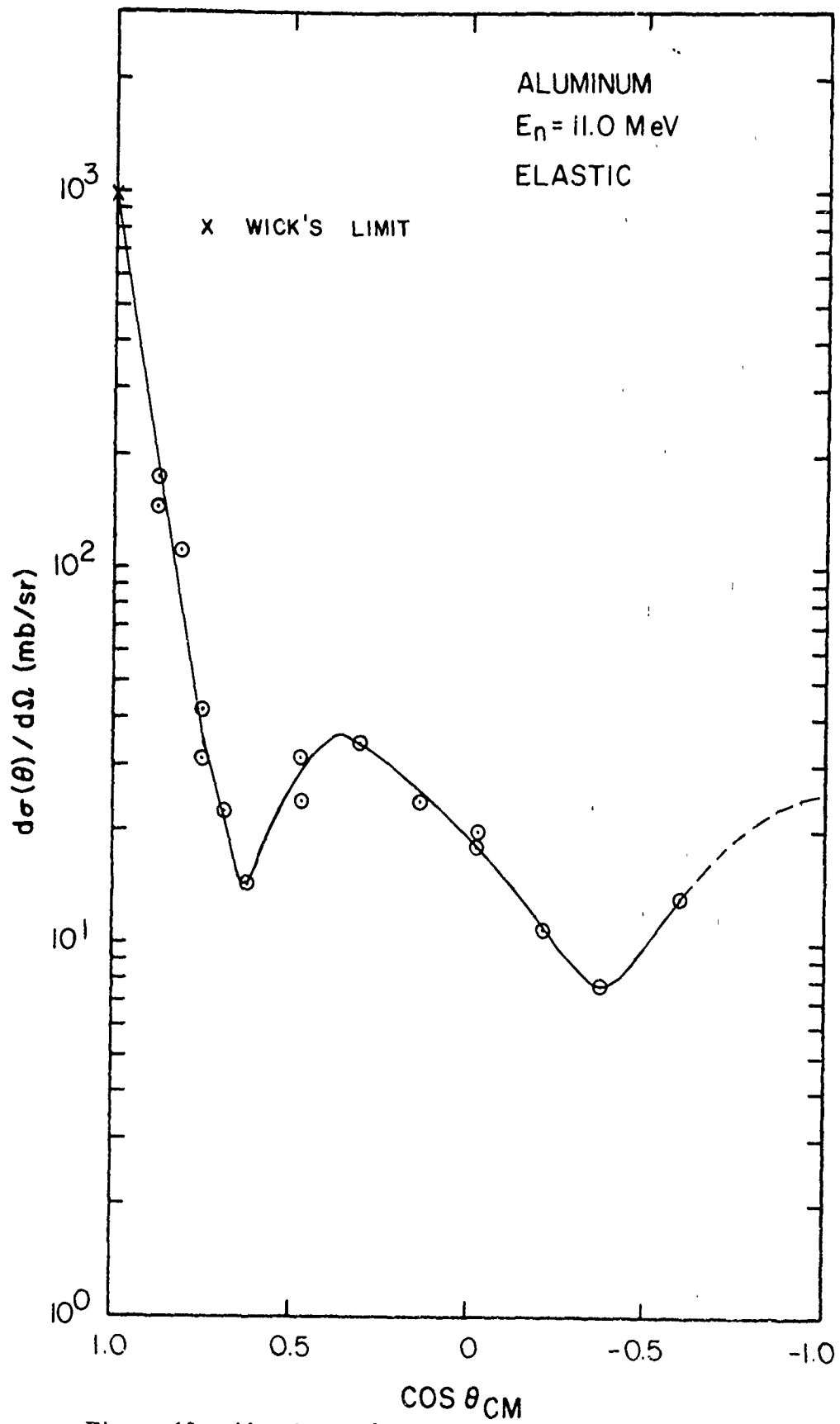


Figure 19. Aluminum elastic scattering at  $E_n = 11.0$  MeV.

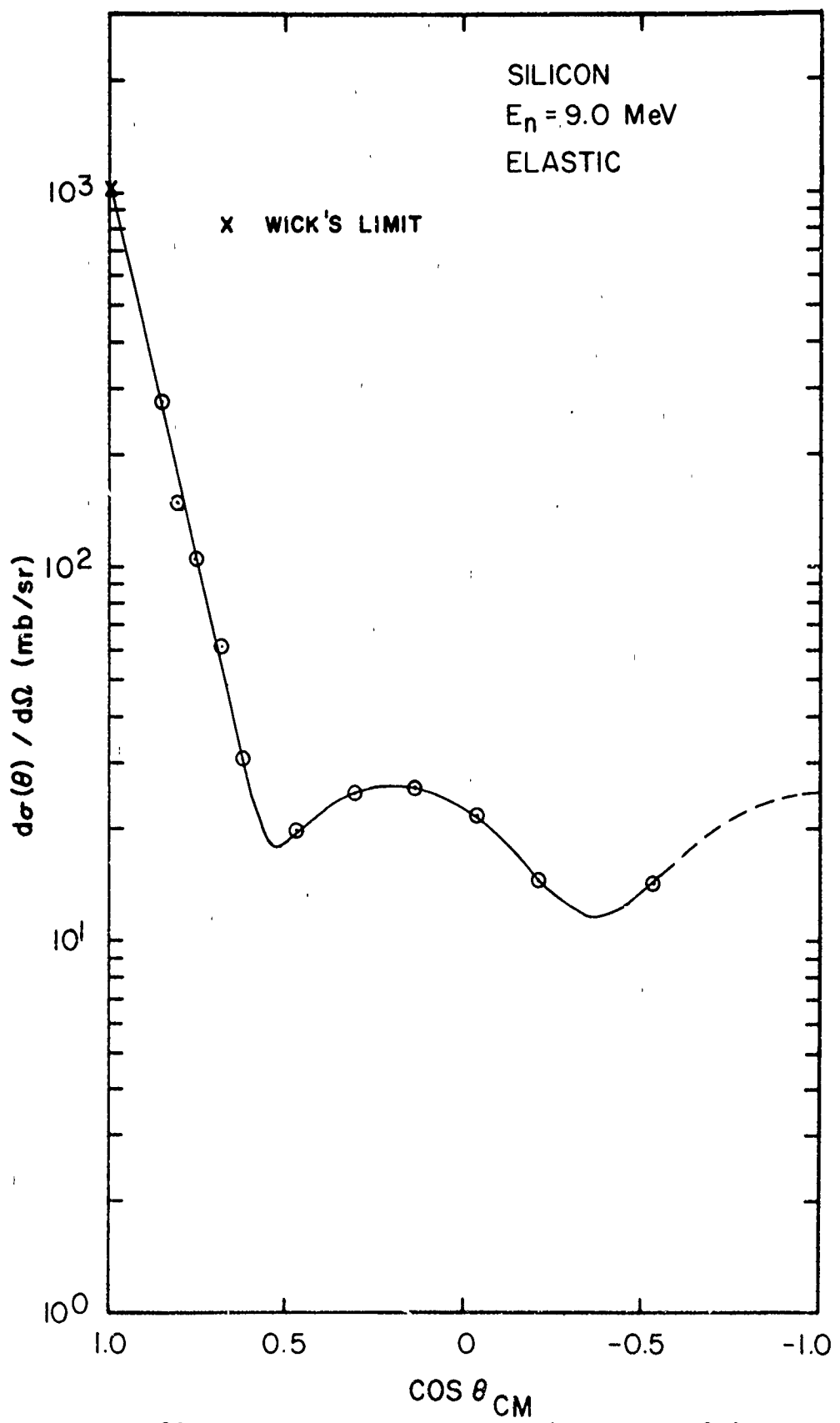


Figure 20. Silicon elastic scattering at  $E_n = 9.0$  MeV.

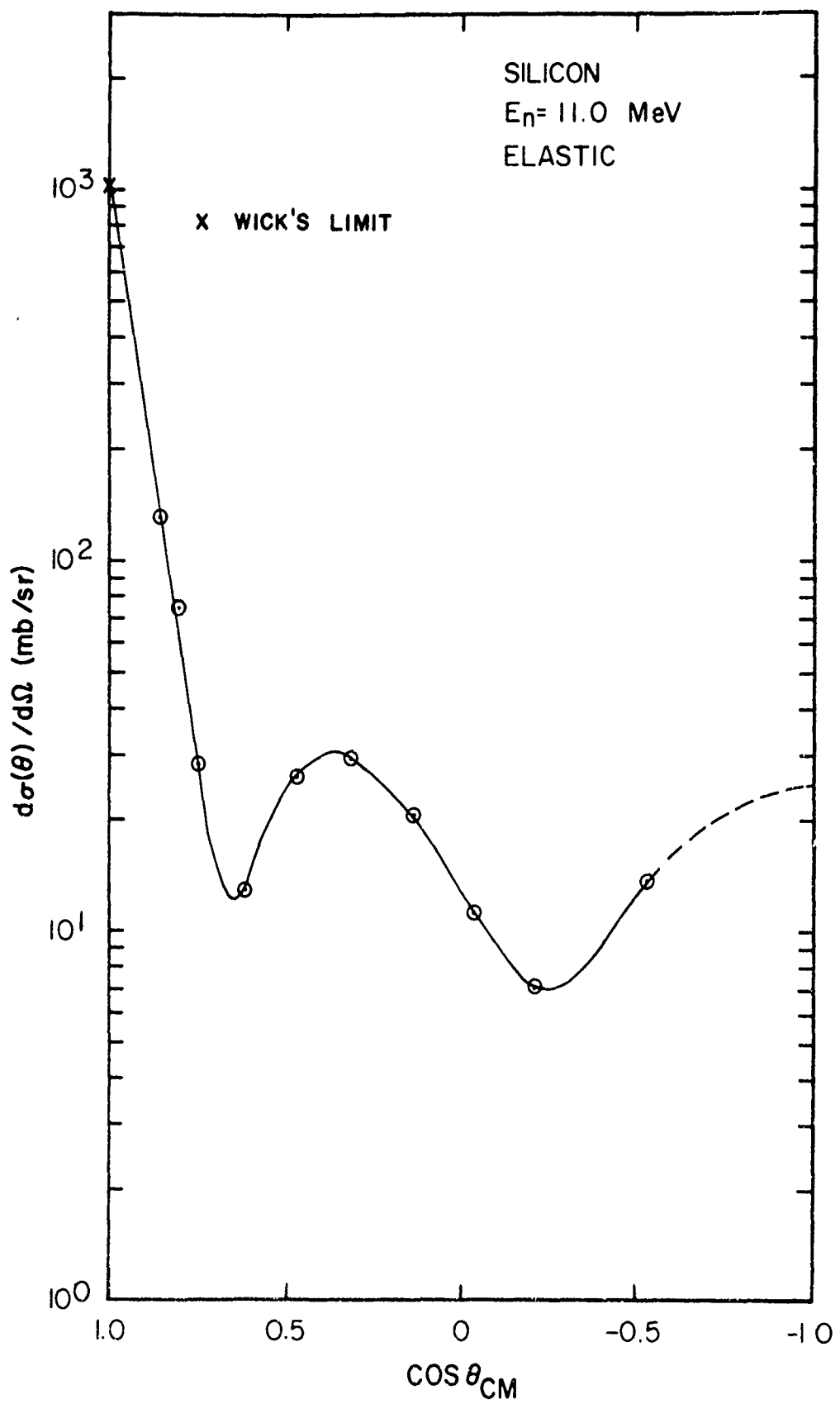


Figure 21. Silicon elastic scattering at  $E_n = 11.0$  MeV.

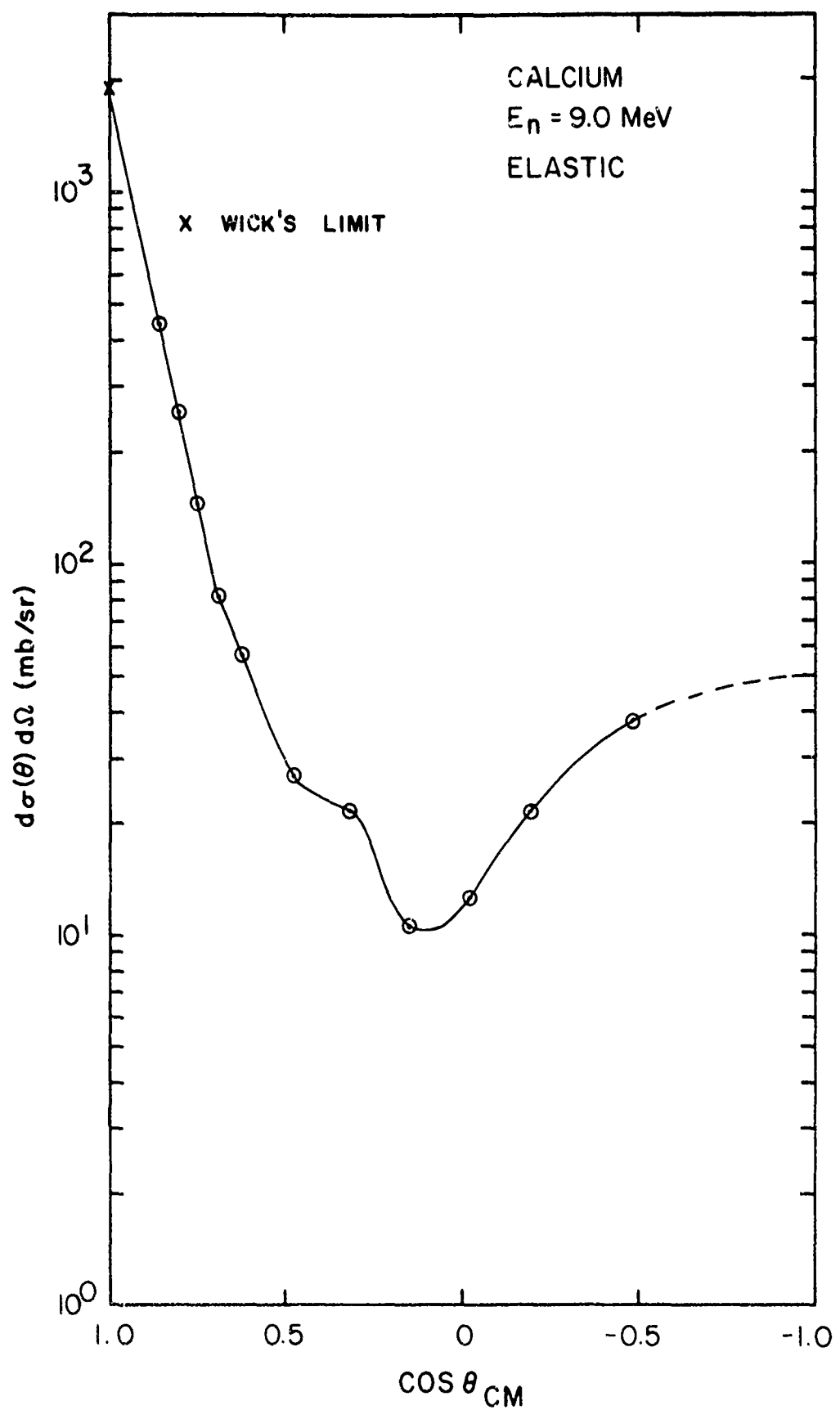


Figure 22. Calcium elastic scattering at  $E_n = 9.0$  MeV.

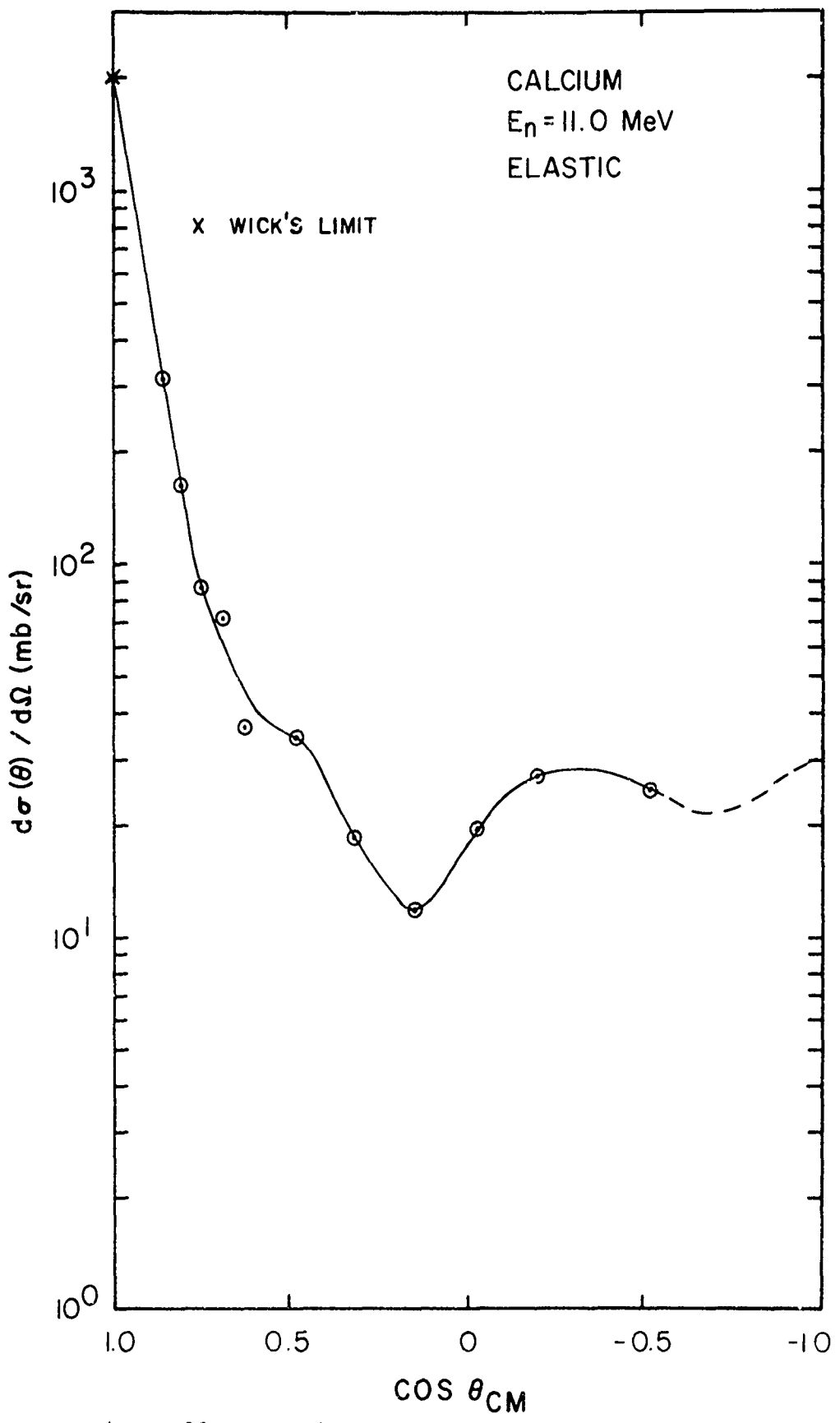


Figure 23. Calcium elastic scattering at  $E_n = 11.0$  MeV.

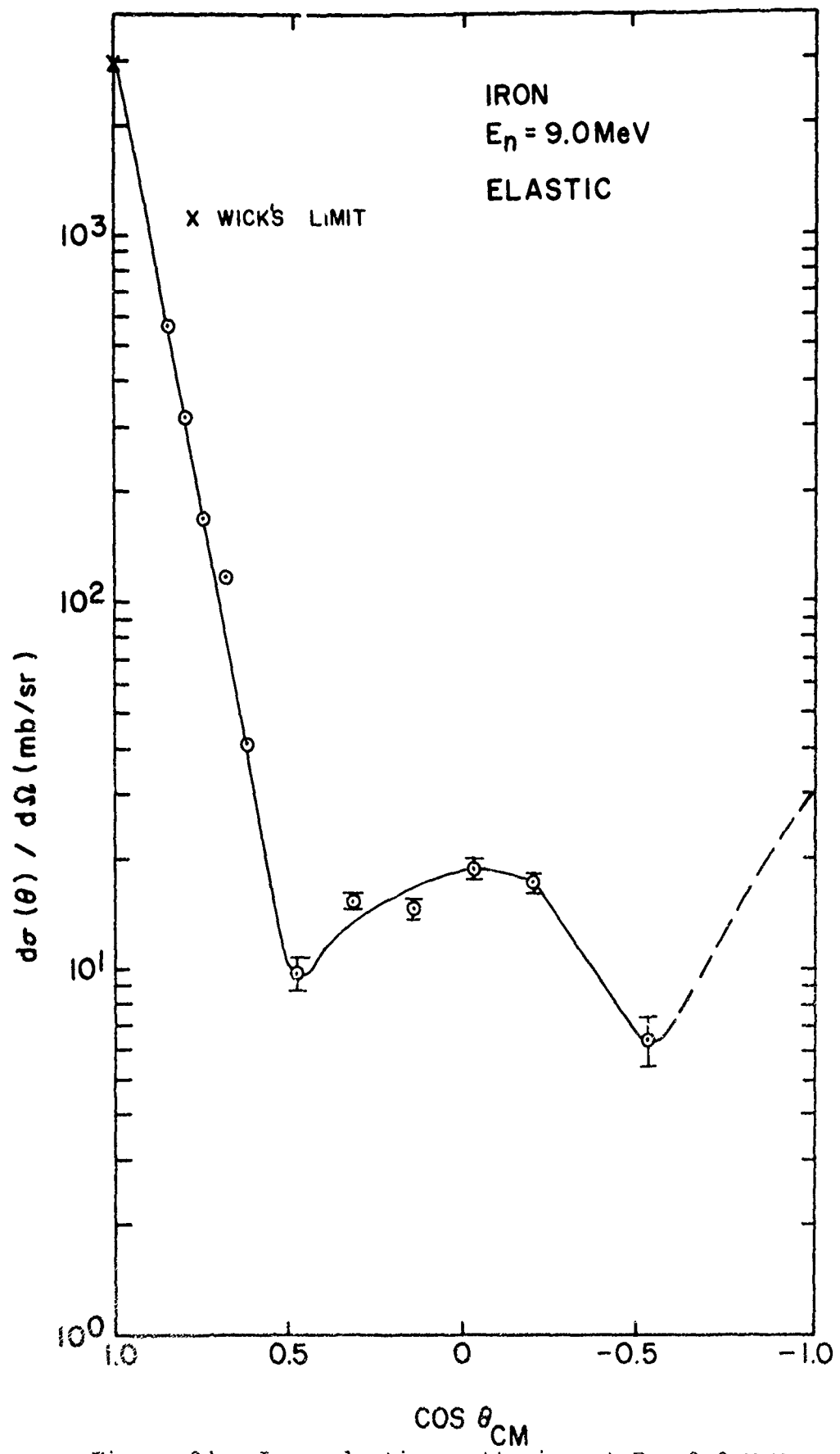


Figure 24. Iron elastic scattering at  $E_n = 9.0 \text{ MeV}$ .

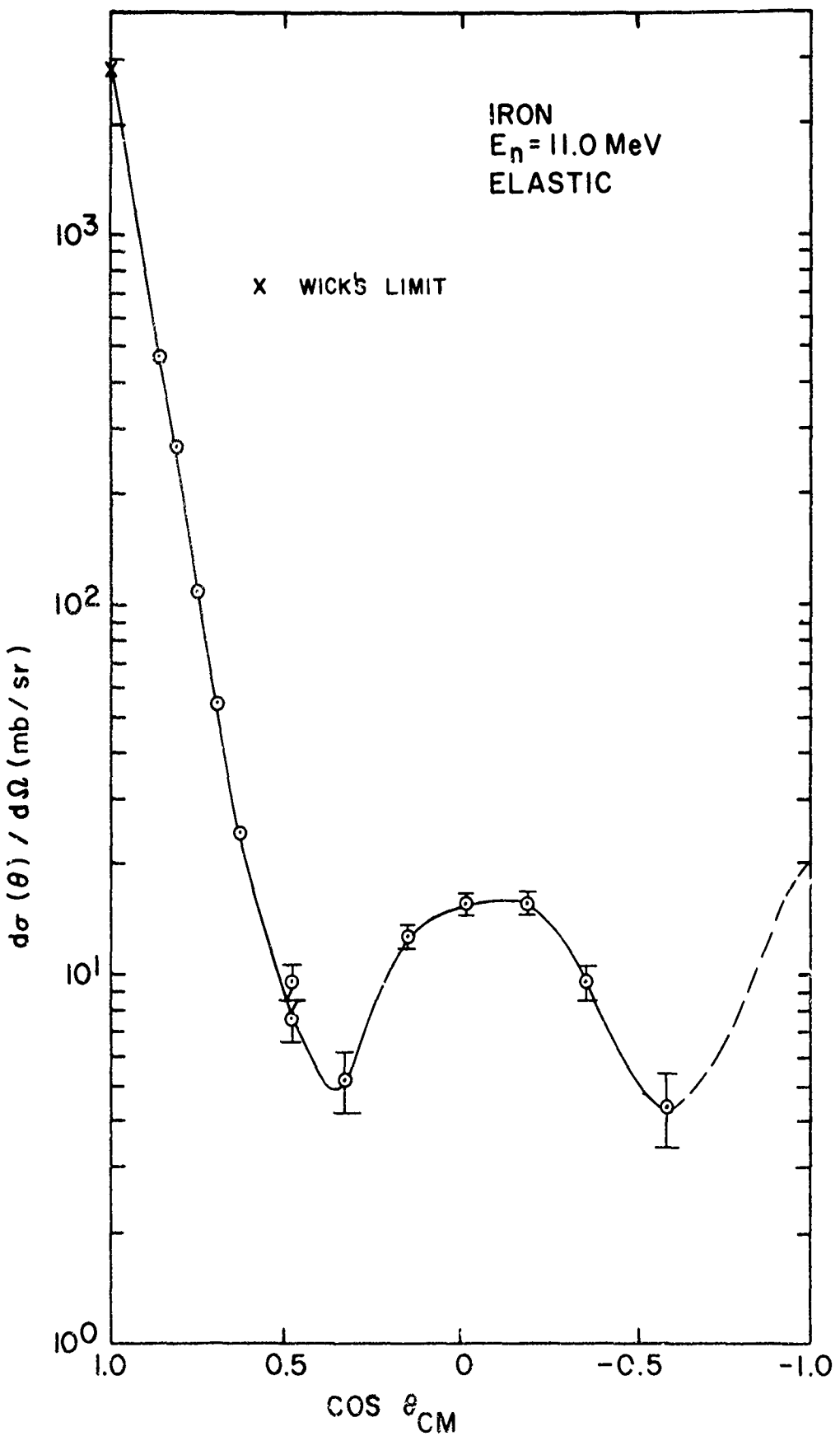


Figure 25 Iron elastic scattering at  $E_n = 11.0$  MeV.

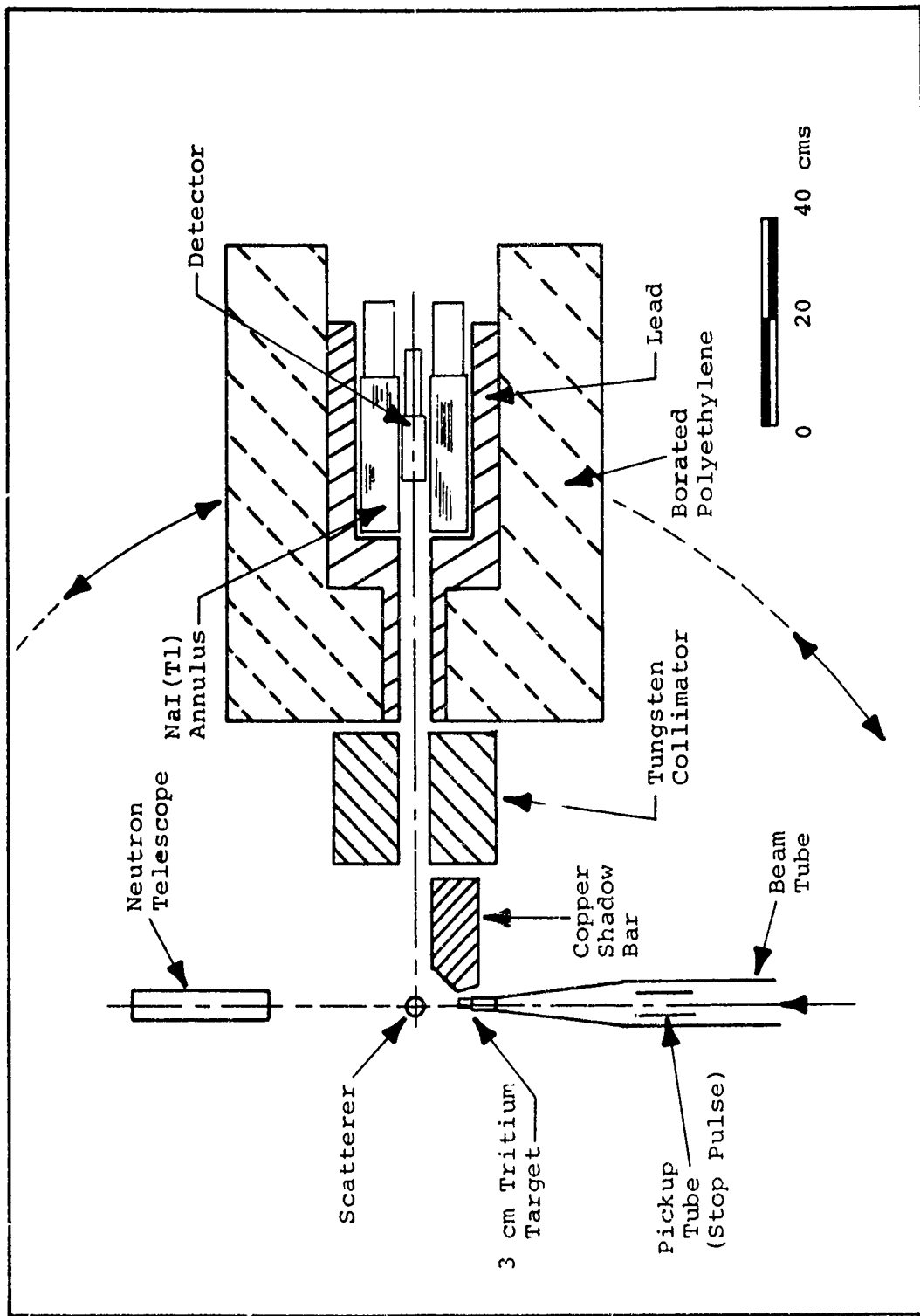


Figure 26. Gamma-ray spectrometer arrangement used at LASL.

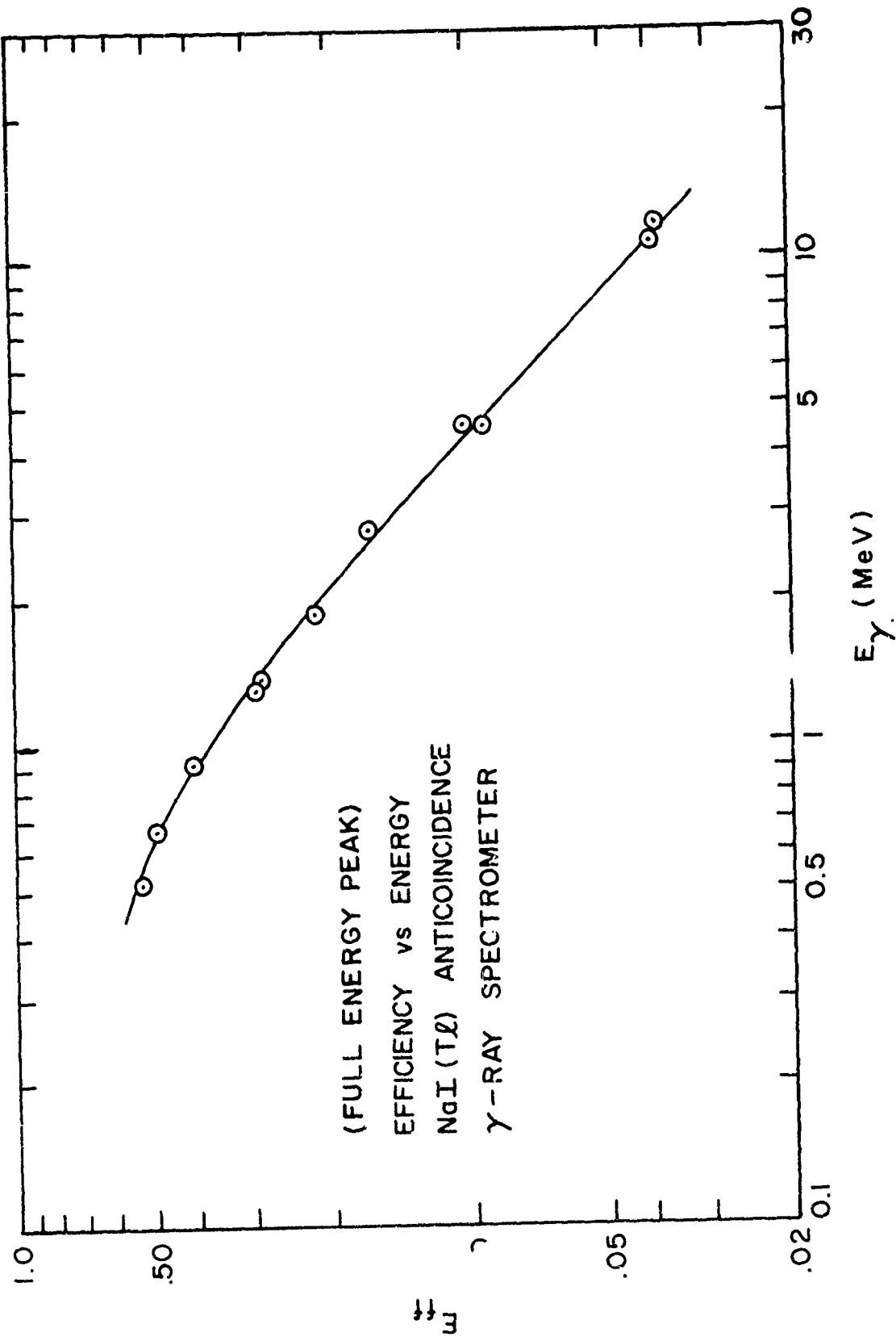


Figure 27. Full Energy Peak Efficiency of the Gamma Ray Detector.

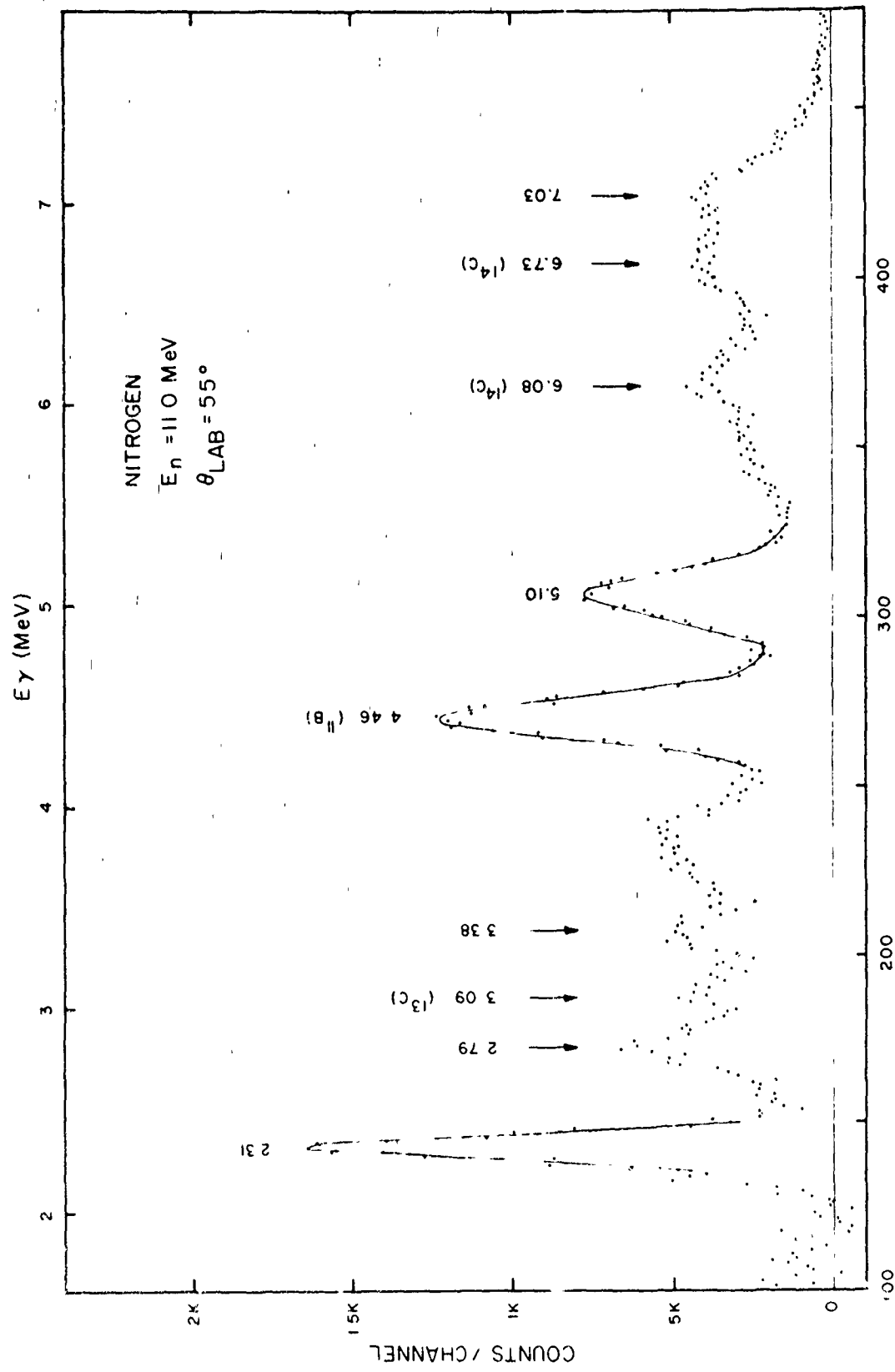


Figure 28. Nitrogen gamma-ray spectrum at  $E_n = 11.0$  MeV.

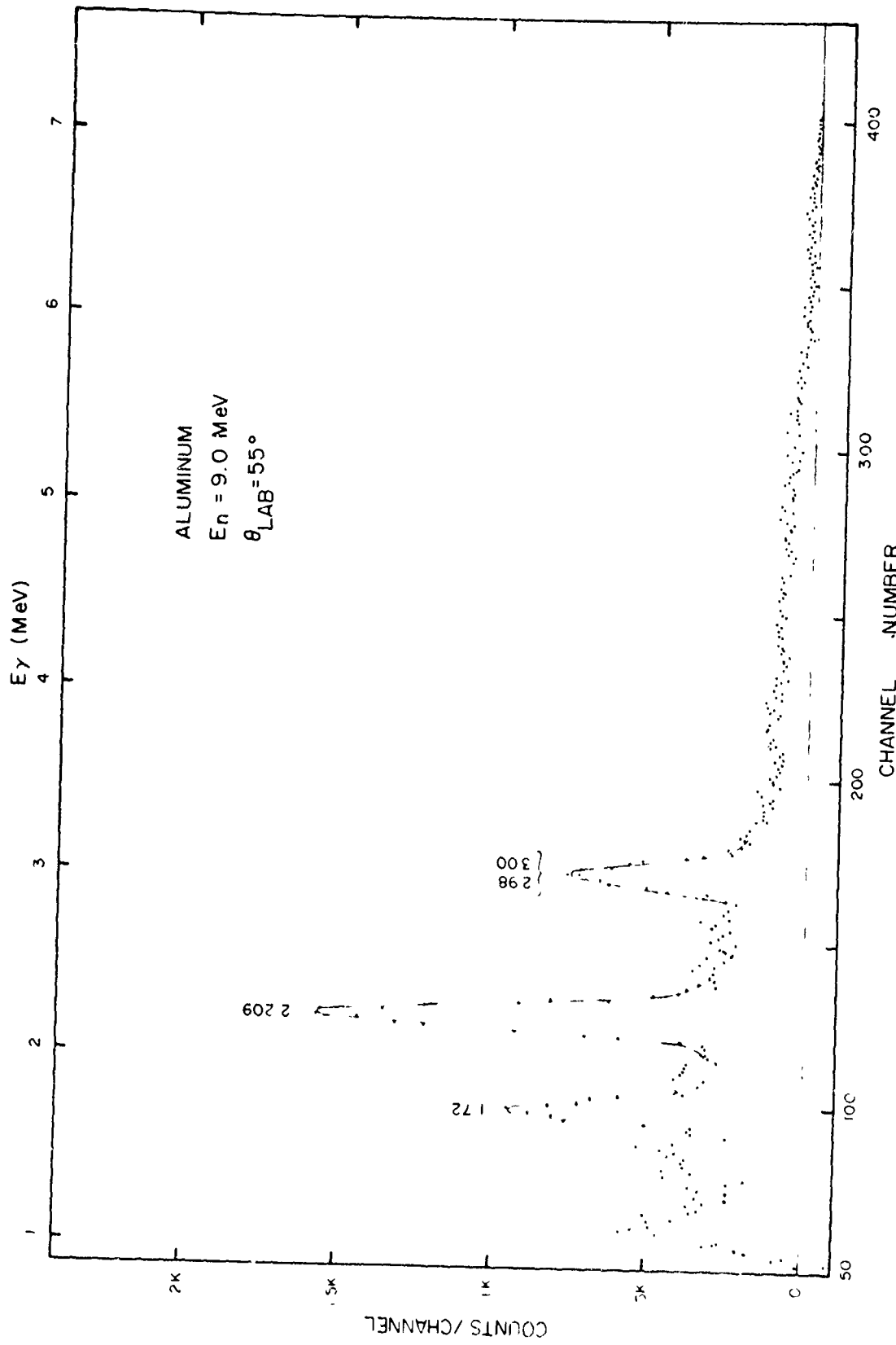


Figure 29. Aluminum gamma-ray spectrum at  $E_n = 9.0$  MeV.

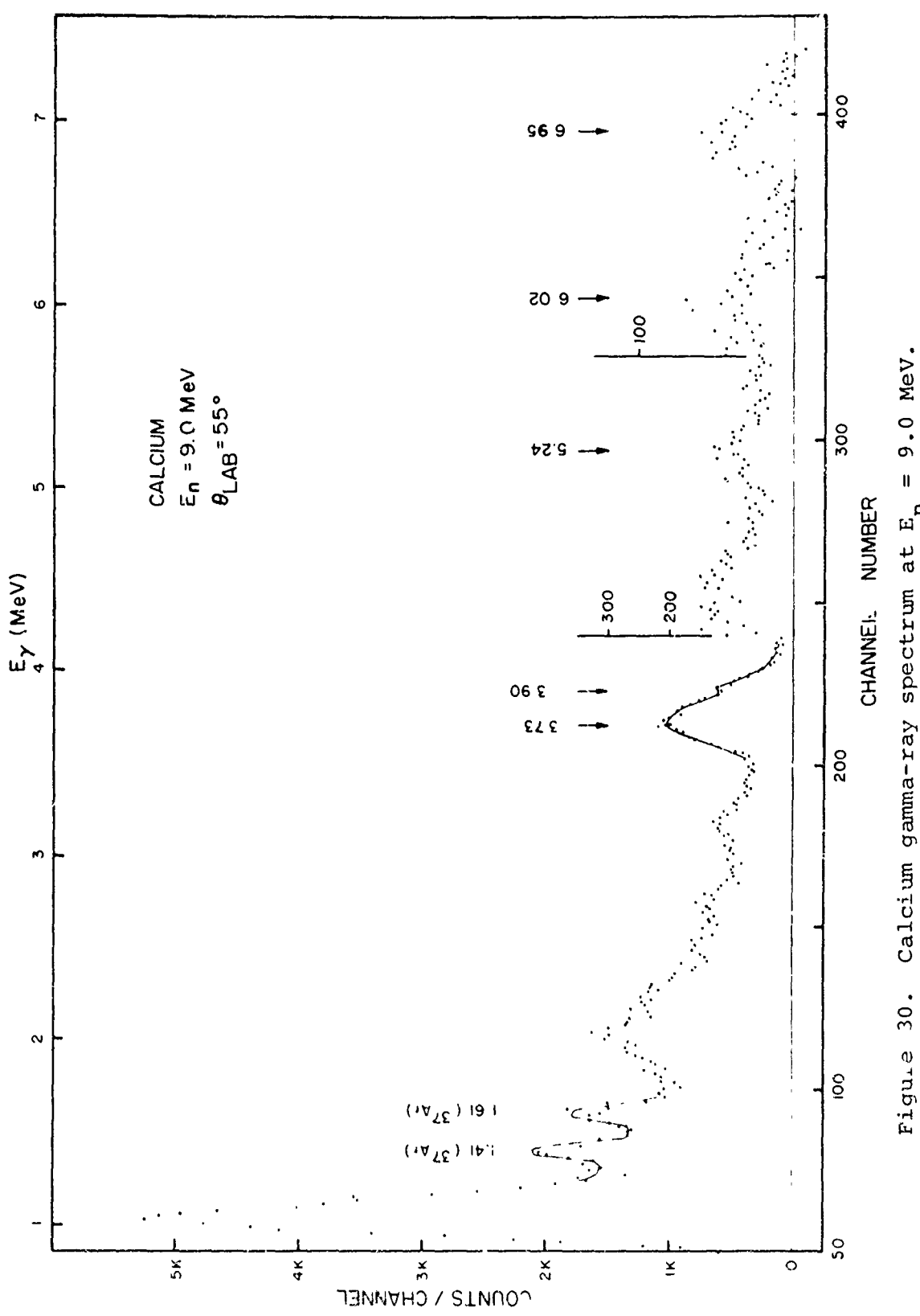


Figure 30. Calcium gamma-ray spectrum at  $E_n = 9.0$  MeV.

TABLE 1

## NITROGEN

## Elastic Scattering of 9.0 MeV Neutrons

$\theta_{\text{cm}}$ (°)	$d\sigma(\theta)/d\Omega$ (mb/sr) $\pm$ 3%
32.1	215.3
32.1	214.0
32.1	183.6
37.3	133.4
42.7	111.3
47.9	86.7
53.2	53.4
63.6	22.0
73.9	34.3
84.0	46.6
94.1	61.8
94.1	72.5
104.1	67.5
113.9	61.0
123.6	43.5
128.4	36.1
Integrated cross section	932 mb $\pm$ 8.8%
Wick's limit	380 mb/sr
Total cross section	1260 mb

TABLE 2

## NITROGEN

Elastic Scattering of 11.0 MeV Neutrons

$\theta_{\text{cm}}$ (°)	$d\sigma(\theta)/d\Omega$ (mb/sr) $\pm$ 3%
32.1	209.1
32.1	202.4
37.3	124.7
42.6	79.2
47.9	46.2
53.2	34.2
63.6	25.8
68.7	26.5
73.9	36.4
79.0	38.8
84.0	55.9
94.1	48.4
94.1	56.3
104.0	46.2
113.9	36.5
123.5	23.7
123.5	25.5
128.4	20.6
Integrated cross section	864 mb $\pm$ 8.8%
Wick's limit	535 mb/sr
Total cross section	1352 mb

TABLE 3

## OXYGEN

Elastic Scattering of 9.0 MeV Neutrons

$\theta_{\text{cm}}$ (°)	$d\sigma(\theta)/d\Omega$ (mb/sr) $\pm$ 3%
31.8	111.1
37.1	102.1
42.3	81.2
47.5	64.0
52.7	33.4
63.1	20.8
73.4	29.8
83.5	63.6
93.6	69.0
103.5	63.7
123.1	37.1
127.9	27.4
Integrated cross section	737 mb $\pm$ 8.8%
Wick's limit	294.5 mb/sr
Total cross section	1100 mb

TABLE 4

## OXYGEN

## Elastic Scattering of 11.0 MeV Neutrons

$\theta_{\text{cm}}$ (°)	$d\sigma(\theta)/d\Omega$ (mb/sr) $\pm$ 3%
31.8	115.9
37.1	85.2
42.3	60.5
47.5	41.4
52.7	31.9
52.7	28.7
63.1	25.6
73.4	23.3
73.4	26.
83.5	37.1
93.6	55.6
103.5	67.1
113.4	54.4
123.1	36.2
Integrated cross section	819 mb $\pm$ 8.8%
Wick's limit	669.4 mb/sr
Total cross section	1500 mb

TABLE 5

## ALUMINUM

Elastic Scattering of 9.0 MeV Neutrons

$\theta_{\text{cm}}$ (°)	$d\sigma(\theta)/d\Omega$ (mb/sr) $\pm$ 3%
31.1	189.6
36.2	135.3
41.4	69.0
46.5	50.8
51.6	29.3
61.8	21.9
72.0	34.7
82.1	31.6
92.1	26.0
102.1	17.1
121.8	10.6
Integrated cross section	687 mb $\pm$ 8.8%
Wick's limit	756.2 mb/sr
Total cross section	1720 mb

TABLE 6

## ALUMINUM

Elastic Scattering of 11.0 MeV Neutrons

$\theta_{\text{cm}}$ (°)	$d\sigma(\theta)/d\Omega$ (mb/sr) $\pm$ 3%
31.1	143.9
31.1	172.4
36.2	110.7
41.4	42.0
41.4	31.1
46.5	22.6
51.6	14.4
61.8	31.0
61.8	23.9
72.0	34.2
82.1	23.9
92.1	18.4
92.1	19.8
102.1	11.0
112.0	7.7
126.7	13.3
Integrated cross section	623 mb $\pm$ 8.8%
Wick's limit	967.7 mb/sr
Total cross section	1760 mb

TABLE 7

## SILICON

## Elastic Scattering of 9.0 MeV Neutrons

$\theta_{\text{cm}}$ (°)	$d\sigma(\theta)/d\Omega$ (mb/sr) $\pm$ 3%
31.0	276.5
36.2	148.8
41.3	100.5
46.4	61.5
51.6	30.7
61.8	19.9
71.9	24.7
82.0	25.9
92.0	21.9
102.0	14.5
121.8	14.2
Integrated cross section	874 mb $\pm$ 8.8%
Wick's limit	1000.9 mb/sr
Total cross sections	1976 mb

TABLE 8

## SILICON

Elastic Scattering of 11.0 MeV Neutrons

$\theta_{\text{cm}}$ (°)	$d\sigma(\theta)/d\Omega$ (mb/sr) $\pm$ 3%
31.0	131.6
36.2	75.0
41.3	28.1
51.6	12.9
61.8	26.0
71.9	29.1
82.0	20.5
92.0	11.1
102.0	7.2
121.8	13.9
Integrated cross section	604 mb $\pm$ 8.8%
Wick's limit	1012.8 mb/sr
Total cross section	1798 mb

TABLE 9

## CALCIUM

## Elastic Scattering of 9.0 MeV Neutrons

$\theta$ cm (°)	$d\sigma(\theta)/d\Omega$ (mb/sr) $\pm$ 3%
30.7	444.9
35.8	257.4
40.9	143.6
46.0	82.9
51.1	56.3
61.2	26.8
71.3	21.5
81.4	10.5
91.4	12.4
102.0	21.6
121.2	37.4
Integrated cross section	1376 mb $\pm$ 8.8%
Wick's limit	1908.1 mb/sr
Total cross section	2700 mb

TABLE 10

## CALCIUM

## Elastic Scattering of 11.0 MeV Neutrons

$\theta_{\text{cm}}$ (°)	$d\sigma(\theta)/d\Omega$ (mb/sr) $\pm$ 3%
30.7	314.8
35.8	161.8
40.9	86.7
46.0	71.7
51.1	36.2
61.2	34.5
71.3	18.4
81.4	11.8
91.4	19.4
101.4	27.0
121.2	24.9
Integrated cross section	1158 mb $\pm$ 8.8%
Wick's limit	1999.4 mb/sr
Total cross section	2500 mb

TABLE II

## IRON

## Elastic Scattering of 9.0 MeV Neutrons

$\theta_{\text{cm}}$ (°)	$d\sigma(\theta)/d\Omega$ (mb/sr)
30.5	565.6 $\pm$ 1%
35.6	319.5 $\pm$ 1%
40.7	168.1 $\pm$ 1%
45.7	116.6 $\pm$ 2%
50.8	40.5 $\pm$ 3%
60.9	9.7 $\pm$ 11%
71.0	15.1 $\pm$ 7%
81.0	14.5 $\pm$ 7%
91.0	18.9 $\pm$ 6%
101.0	17.3 $\pm$ 6%
120.9	6.4 $\pm$ 16%
Integrated cross section	1672 mb $\pm$ 8.8%
Wick's limit	2872.8 mb/sr
Total cross section	3290 mb

TABLE 12

## IRON

## Elastic Scattering of 11.0 MeV Neutrons

$\theta_{\text{cm}}$ (°)	$d\sigma(\theta)/d\Omega$ (mb/sr)
30.5	467.8 ± 1%
35.6	266.0 ± 1%
40.7	109.1 ± 2%
45.7	54.1 ± 3%
50.8	24.0 ± 4%
60.9	9.5 ± 11%
60.9	7.6 ± 14%
71.0	5.2 ± 20%
81.0	12.7 ± 8%
91.0	15.7 ± 7%
91.0	15.7 ± 7%
101.0	15.9 ± 7%
111.0	9.6 ± 11%
125.8	4.4 ± 23%
Integrated cross section	1369 mb ± 8.8%
Wick's limit	2886.3 mb/sr
Total cross section	2930 mb

TABLE 13

## NITROGEN

Inelastic Scattering of 9.0 MeV Neutrons

Average of  $\theta_{\text{lab}} = 90^\circ$  and  $\theta_{\text{lab}} = 125^\circ$ 

$E_{\text{ex}}$ (MeV)	$d\sigma(\theta)/d\Omega$ (mb/sr)	Error (± %)
3.945	4.77	4
4.913		
5.106 }	6.39	5
5.691		
5.834 }	5.00	10
6.198		
6.444 }	6.70	10
7.028	4.64	10
<hr/>		
Sum	27.50 mb/sr ± 7.8%	
Integrated ( $4\pi \times \text{sum}$ )	346 mb ± 11%	

TABLE 14

## NITROGEN

Inelastic Scattering of 11.0 MeV Neutrons

Average of  $\theta_{\text{lab}} = 70^\circ$  and  $\theta_{\text{lab}} = 120^\circ$ 

$E_{\text{ex}}$ (MeV)	$d\sigma(\theta)/d\Omega$ (mb/sr)	Error ( $\pm$ %)
3.945	1.97	7
4.913		
5.106 }	2.71	8
5.691		
5.834 }	2.73	8
6.198		
6.444 }	3.10	10
7.028	4.20	10
7.966		
8.061 }	4.04	10
8.488		
8.617 }	3.84	10
<hr/>		
Sum	22.59 mb/sr $\pm$ 8.9%	
Integrated ( $4\pi \times \text{sum}$ )	284 mb $\pm$ 12%	

TABLE 15

## OXYGEN

Inelastic Scattering of 9.0 MeV Neutrons  
to the 6.06 and 6.13 MeV Levels

$\theta_{cm}$ ( $^{\circ}$ )	$d\sigma(\theta)/d\Omega$ (mb/sr)	Error ( $\pm \%$ )
33.4	17.1	14
38.9	17.1	11
44.4	21.1	19
49.8	21.6	13
76.4	17.9	8
86.7	20.6	10
96.8	17.7	3
106.7	13.9	3
125.9	16.2	8
130.6	14.8	5
Average	17.8	10

---

Integrated ( $4\pi \times$  average)      224 mb  $\pm$  13%

TABLE 16

## OXYGEN

Inelastic Scattering of 11.0 MeV Neutrons  
to the 6.06 and 6.13 MeV Levels

$\theta$ cm (°)	$d\sigma(\theta)/d\Omega$ (mb/sr)	Error (± %)
32.8	9.8	25
38.2	10.1	14
43.6	11.0	20
64.8	9.2	11
75.2	8.8	4
85.5	9.1	5
95.5	7.8	5
105.5	8.0	4
115.2	9.2	5
124.8	8.5	8
Average	9.2	9.8

---

Integrated ( $4\pi \times$  average) 116 mb ±13%

TABLE 17

## OXYGEN

Inelastic Scattering of 11.0 MeV Neutrons  
of the 6.92 and 7.12 MeV Levels

$\theta$ cm (°)	$d\sigma(\theta)/d\Omega$ (mb/sr)	Error (± %)
32.8	15.5	22
38.2	13.2	13
43.6	15.3	16
48.9	18.8	14
75.2	16.6	4
85.5	15.8	6
95.5	14.4	4
105.5	15.7	4
115.2	16.5	4
124.8	14.4	6
Average	15.6	9

---

Integrated ( $4\pi \times$  average) 196 mb ± 12%

TABLE 18

## ALUMINUM

Inelastic Scattering of 9.0 MeV Neutrons

$$\theta_{\text{lab}} = 90^\circ$$

$E_n$ , (MeV)	$E_{\text{ex}}$ (MeV)	$d\sigma(\theta)/d\Omega$ (mb/sr)	Error (± %)
	2.209		
	2.732		
	2.980	14.21	3
	3.00		
4.0 - 5.0	4.52 - 3.48	5.68	4
3.0 - 4.0	5.56 - 4.52	10.09	3
2.5 - 3.0	6.07 - 5.56	6.87	3
2.0 - 2.5	6.59 - 6.07	6.44	3
1.5 - 2.0	7.11 - 6.07	11.06	3
<hr/>			
Sum		54.35 mb/sr ± 3%	
Integrated ( $4\pi \times \text{sum}$ )		683 mb ± 8.8%	

TABLE 19

## ALUMINUM

Inelastic Scattering of 11.0 MeV Neutrons

$$\theta_{\text{lab}} = 70^{\circ}$$

$E_n$ , (MeV)	$E_{\text{ex}}$ (MeV)	$d\sigma(\theta)/d\Omega$ (mb/sr)	Error (± %)
	2.209		
	2.732	10.72	3
	2.980		
	3.00		
6.0 - 7.0	4.58 - 3.56	2.24	8
5.0 - 6.0	5.60 - 4.58	4.75	4
4.0 - 5.0	6.61 - 5.60	6.67	3
3.5 - 4.0	7.12 - 6.61	5.55	2
3.0 - 3.5	7.63 - 7.12	7.41	2
2.5 - 3.0	8.13 - 7.63	7.64	2
2.0 - 2.5	8.64 - 8.13	8.19	3
1.5 - 2.0	9.14 - 8.64	6.07	5
<hr/>			
Sum		59.24 mb/sr ± 3%	
Integrated ( $4\pi \times \text{sum}$ )		744 mb ± 8.8%	

TABLE 20

## SILICON

Inelastic Scattering of 9.0 MeV Neutrons

$$\theta_{\text{lab}} = 90^\circ$$

$E_{\text{ex}}$ (MeV)	$d\sigma(\theta)/d\Omega$ (mb/sr)	Error (± %)
1.779	17.5	2
4.617		
4.975 }	9.39	3
6.276	6.22	5
6.69	2.98	6
6.878		
6.889 }	11.90	6
7.38		
7.416 }	8.18	6
<hr/>		
Sum	56.17 mb/sr ± 4%	
Integrated ( $4\pi \times \text{sum}$ )	706 mb ± 9.1%	

TABLE 21

## SILICON

## Inelastic Scattering of 11.0 MeV Neutrons

 $\theta_{\text{lab}} = 70^\circ$ 

$E_{\text{ex}}$ (MeV)	$d\sigma(\theta)/d\Omega$ (mb/sr)	Error (± %)
1.779	12.68	2
4.617		
4.975 }	5.51	4
6.276	3.51	4
6.878		
6.889 }	9.18	3
7.38		
7.416 }	6.91	3
7.798		
7.935 }	7.17	3

Sum  $44.96 \text{ mb/sr} \pm 3\%$ Integrated  $565 \text{ mb} \pm 8.8\%$   
( $4\pi \times \text{sum}$ )

TABLE 22

## CALCIUM

Inelastic Scattering of 9.0 MeV Neutrons

$$\theta_{\text{lab}} = 90^\circ$$

$E_n$ (MeV)	$E_{\text{ex}}$ (MeV)	$d\sigma(\theta)/d\Omega$ (mb/sr)	Error (± %)
	3.351		
	3.734	8.45	6
	3.903		
	4.487		
3.5 - 3.8	5.18 - 4.88	1.31	12
3.0 - 3.5	5.70 - 5.18	3.17	7
2.5 - 3.0	6.21 - 5.70	2.74	8
2.0 - 2.5	6.72 - 6.21	5.21	6
1.5 - 2.0	7.23 - 6.72	5.44	7
<hr/>			
Sum		26.32 mb/sr ± 6%	
Integrated ( $4\pi \times \text{sum}$ )		331 mb ± 10%	

TABLE 23

## CALCIUM

Inelastic Scattering of 11.0 MeV Neutrons

$$\theta_{\text{lab}} = 70^\circ$$

$E_n$ , (MeV)	$E_{\text{ex}}$ (MeV)	$d\sigma(\theta)/d\Omega$ (mb/sr)	Error ( $\pm \%$ )
	3.351		
	3.734	10.70	5
	3.903		
	4.487		
5.0 - 5.8	5.73 - 4.92	2.61	13
4.5 - 5.0	6.23 - 5.73	1.57	12
4.0 - 4.5	6.74 - 6.23	3.61	6
3.5 - 4.0	7.24 - 6.74	4.27	5
3.0 - 3.5	7.74 - 7.24	6.06	4
2.5 - 3.0	8.25 - 7.74	6.66	5
2.0 - 2.5	8.75 - 8.25	9.04	4
1.5 - 2.0	9.26 - 8.75	13.71	4
<hr/>			
Sum		58.23 mb/sr $\pm$ 5%	
Integrated ( $4\pi \times \text{sum}$ )		732 mb $\pm$ 10%	

TABLE 24

## IRON

Inelastic Scattering of 9.0 MeV Neutrons

$$\theta_{\text{lab}} = 90^\circ$$

$E_n'$ (MeV)	$E_{\text{ex}}$ (MeV)	$d\sigma(\theta)/d\Omega$ (mb/sr)	Error (± %)
7.85	0.845	6.0	20
6.0 - 7.2	2.73 - 1.49	4.04	8
5.5 - 6.0	3.24 - 2.73	3.65	3
5.0 - 5.5	3.75 - 3.24	3.24	3
4.5 - 5.0	4.26 - 3.75	4.12	2
4.0 - 4.5	4.77 - 4.26	6.12	2
3.5 - 4.0	5.27 - 4.77	7.08	2
3.0 - 3.5	5.78 - 5.27	8.66	2
2.5 - 3.0	6.29 - 5.78	11.23	2
2.0 - 2.5	6.80 - 6.29	14.05	2
1.5 - 2.0	7.31 - 6.80	17.91	2
Total		86.10 mb/sr ± 3.6%	
Integrated ( $4\pi \times \text{total}$ )		1082 mb ± 8.9%	

TABLE 25

## IRON

Inelastic Scattering of 11.0 MeV Neutrons

$$\theta_{\text{lab}} = 70^\circ$$

$E_n'$ (MeV)	$E_{\text{ex}}$ (MeV)	$d\sigma(\theta)/d\Omega$ (mb/sr)	Error (± %)
10.6	.845	6.0	17
8.7	2.084	1.52	14
7.0 - 8.5	3.57 - 2.27	4.50	7
6.5 - 7.0	3.78 - 3.57	1.37	9
6.0 - 6.5	4.79 - 3.78	2.31	6
5.5 - 6.0	5.30 - 4.79	3.37	4
5.0 - 5.5	5.80 - 5.30	2.32	4
4.5 - 5.0	6.31 - 5.80	4.13	3
4.0 - 4.5	6.81 - 6.31	4.62	3
3.5 - 4.0	7.31 - 6.81	6.35	2
3.0 - 3.5	7.82 - 7.31	8.21	2
2.5 - 3.0	8.23 - 7.82	10.62	2
2.0 - 2.5	8.82 - 8.23	14.08	2
1.5 - 2.0	9.32 - 8.32	14.56	2
Total		83.92 mb/sr ± 4%	
Integrated ( $4\pi \times \text{total}$ )		1055 mb ± 9.1%	

TABLE 26

## NITROGEN

Gamma-Ray Production Cross Sections for 11 MeV Neutrons

$E_{\gamma}$ (MeV)	$d\sigma(55^\circ)/d\Omega$ (mb/sr) $\pm$ 20%	$\gamma$ ray origin
2.31	2.71	$^{14}\text{N}$
2.5 - 3.0	.63	
3.0 - 3.5	.94	
3.5 - 4.0	1.90	$^{13}\text{C}$
4.46	5.83	$^{11}\text{B}$
5.1	4.29	$^{14}\text{N}$
5.4 - 6.0	1.69	
6.0 - 6.5	3.12	
6.5 - 7.0	5.62	
7.0 - 7.5	3.12	
7.5 - 7.75	0.37	
<hr/>		
Total	30.22 mb/sr $\pm$ 20%	
Integrated ( $4\pi \times$ total)	380 mb $\pm$ 20%	

TABLE 27

## OXYGEN

Gamma-Ray Production Cross Sections for 11 MeV Neutrons

$E_{\gamma}$ (MeV)	$d\sigma(55^\circ)/d\Omega$ (mb/sr) $\pm$ 20%	$\gamma$ ray origin
3.68		
3.86	4.22	$^{13}\text{C}$
6.13	6.85	$^{16}\text{O}$
6.92		
7.12	8.47	$^{16}\text{O}$
Total	19.54 mb/sr $\pm$ 20%	
Integrated ( $4\pi \times$ total)	246 mb $\pm$ 20%	

TABLE 28

## ALUMINUM

Gamma-Ray Production Cross Sections for 9.0 MeV Neutrons

$E_{\gamma}$ (MeV)	$d\sigma(55^\circ)/d\Omega$ (mb/sr) $\pm$ 20%	$\gamma$ ray origin
1.72	6.99	$^{27}\text{Al}$
1.9 - 2.1	1.59	
2.209	21.12	$^{27}\text{Al}$
2.4 - 2.8	6.13	
2.98		
3.00 }	13.97	$^{27}\text{Al}$
3.15 - 3.5	3.17	
3.5 - 4.0	3.22	
4.0 - 4.5	3.73	
4.5 - 5.0	3.96	
5.0 - 5.5	4.59	
5.5 - 6.0	3.22	
6.0 - 6.5	2.61	
6.5 - 7.0	1.89	
Total	76.19 mb/sr $\pm$ 20%	
Integrated ( $4\pi \times$ total)	957 mb $\pm$ 20%	

TABLE 29

## ALUMINUM

Gamma-Ray Production Cross Sections for 11.0 MeV Neutrons

$E_{\gamma}$ (MeV)	$d\sigma(55^\circ)/d\Omega$ (mb/sr) $\pm 20\%$	$\gamma$ ray origin
1.5 - 2.0	6.52	
2.209	8.89	$^{27}\text{Al}$
2.4 - 2.8	2.52	
2.98		
3.00 }	9.84	$^{27}\text{Al}$
3.2 - 3.5	1.36	
3.5 - 4.0	2.74	
4.0 - 4.5	3.61	
4.5 - 5.0	3.16	
5.0 - 5.5	3.48	
5.5 - 6.0	3.15	
6.0 - 6.5	2.50	
6.5 - 7.0	2.60	
7.0 - 7.5	2.41	
Total	52.78 mb/sr $\pm 20\%$	
Integrated ( $4\pi \times$ total)	663 mb $\pm 20\%$	

TABLE 30

## CALCIUM

Gamma-Ray Production Cross Sections for 9.0 MeV Neutrons

$E_{\gamma}$ (MeV)	$d\sigma(55^\circ)/d\Omega$ (mb/sr) $\pm$ 20%	$\gamma$ ray origin
1.25 - 1.5	10.69	Ca + $^{37}\text{Ar}$
1.5 - 2.0	14.69	Ca + $^{37}\text{Ar}$
2.0 - 2.5	22.57	
2.5 - 3.0	13.55	
3.0 - 3.5	11.86	
3.73 3.90 }	26.36	$^{40}\text{Ca}$
4.2 - 4.5	1.91	
4.5 - 5.0	2.46	
5.0 - 5.5	3.26	
5.5 - 6.0	1.90	
6.0 - 6.5	1.19	
6.5 - 7.0	1.52	
7.0 - 7.5	1.05	
Total	113.01 mb/sr $\pm$ 20%	
Integrated ( $4\pi \times$ total)	1420 mb $\pm$ 20%	

TABLE 31

## CALCIUM

Gamma-Ray Production Cross Section for 11.0 MeV Neutrons

$E_{\gamma}$ (MeV)	$d\sigma(55^\circ)/d\Omega$ (mb/sr) $\pm$ 20%	$\gamma$ ray origin
2.25 - 2.5	7.48	
2.5 - 3.0	13.90	
3.0 - 3.5	15.95	
3.73 }	33.09	$^{40}\text{Ca}$
3.90		
4.2 - 4.5	2.98	
4.5 - 5.0	7.25	
5.0 - 5.5	4.00	
5.5 - 6.0	3.65	
6.0 - 6.5	3.81	
6.5 - 7.0	2.29	
7.0 - 7.5	3.72	
Total	98.12 mb/sr $\pm$ 20%	
Integrated ( $4\pi \times$ total)	1233 mb $\pm$ 20%	

TABLE 32

## IRON

Gamma-Ray Production Cross Sections for 9.0 MeV Neutrons

$E_{\gamma}$ (MeV)	$d\sigma(55^\circ)/d\Omega$ (mb/sr) $\pm$ 20%	$\gamma$ ray origin
1.5 - 2.0	26.23	
2.0 - 2.5	20.39	
2.5 - 3.0	19.41	
3.0 - 3.5	13.16	
3.5 - 4.0	15.48	
4.0 - 4.5	7.46	
4.5 - 5.0	4.96	
5.0 - 5.5	3.85	
5.5 - 6.0	3.85	
6.0 - 6.5	3.65	
6.5 - 7.0	3.29	
7.0 - 7.5	3.31	
Total	125.04 mb/sr $\pm$ 20%	
Integrated ( $4\pi \times$ total)	1570 mb $\pm$ 20%	

1. W. E. Tucker, P. S. Buchanan, T. C. Martin, D. O. Nellis, and G. H. Williams, Defense Atomic Support Agency Report DASA2333, (1969).
2. S. J. Bame, Jr., E. Haddad, J. E. Perry, Jr., and R. K. Smith, Rev. Sci. Instr. 29, 652, (1958).
3. S. J. Bame, Jr., E. Haddad, J. E. Perry, Jr., R. K. Smith, and B. Swartz, Rev. Sci. Instr. 31, 911 (1960).
4. L. Cranberg and J. S. Levin, Los Alamos Scientific Laboratory Report No. LA-2177, 1959 (unpublished).
5. W. E. Wilson, R. L. Walter, and D. B. Fossan, Nucl. Phys. 27, 421 (1961).
6. R. W. Bauer, J. D. Anderson, and L. J. Christensen, Nucl. Phys. 47, 241 (1963).
7. R. W. Bauer, J. D. Anderson, H. F. Lutz, C. Wong, J. W. McClure and B. A. Pohl, Nucl. Phys. A93, 673 (1967).
8. J. R. Stehn, M. D. Goldberg, B. A. Magurno and R. Wiener-Chasman, Neutron Cross Sections BNL 325, May 1961.
9. D. Meier, M. Brüllmann, H. Jung and P. Marmier, Helv. Phys. Acta 42, 813 (1969).
10. J. K. Dickens and F. G. Perey, Nucl. Sci. Eng. 40, 283 (1970).
11. V. J. Orphan, C. G. Hoot, and Joseph John, Nucl. Sci. Eng. 42, 352 (1970).

12. W. E. Kinney and F. G. Perey, Oak Ridge National Laboratory Report ORNL-4516 (1970).
13. W. E. Kinney and F. G. Perey, Oak Ridge National Laboratory Report ORNL-4517 (1970).
14. F. G. Perey and W. E. Kinney, Oak Ridge National Laboratory Report ORNL-4519 (1970).
15. W. E. Kinney and F. G. Perey, Oak Ridge National Laboratory Report ORNL-4515 (1970).
16. J. B. Ashe, J. D. Hall, and I. L. Morgan, Rev. Sci. Instr. 37, 1559 (1966).
17. G. H. Williams, and I. L. Morgan, Nucl. Instr. and Methods 45, 313 (1966).
18. G. E. Thomas, D. E. Blatchley and L. M. Bollinger, Nucl. Instr. and Methods 56, 325 (1967).
19. W. E. Tucker et al, Texas Nuclear Report ORO-2791-33  
15 February 1971.
20. J. K. Dickens and F. G. Perey, Nucl. Sci. Eng. 40, 346 (1970).
21. V. J. Orphan, C. G. Hoot et al, Gulf General Atomic Report GA-8006, 1969 (revised).
22. D. M. Drake, J. C. Hopkins, C. S. Young and H. Conde, Nucl. Sci. Eng. 40, 294 (1970).
23. W. E. Tucker, Phys. Rev. 140, B1541 (1965).

24. S. K. Penny and W. E. Kirney, Oak Ridge National Laboratory Report ORNL-4617 (1971).
25. Oak Ridge National Laboratory Annual Progress Report ORNL-4592 (1970) p. 32.

APPENDIX  
ERRATA FOR REPORT DASA-2333

The document DASA-2333, entitled "Neutron-Induced Gamma-Ray Production Cross Sections For Silicon And Tungsten", was prepared as an interim report of the initial phase of the research accomplished under the current program. Subsequent to the publication of this report, an error was discovered in the determination of the incident neutron flux for a portion of the data reported in the subject document. The rectification of this error has resulted in the reduction, by approximately 18%, of all cross sections reported at  $E_n = 8.0, 9.0, 10.0$ , and  $11.0 \text{ MeV}$ . No correction is required for the  $E_n = 5.0 \text{ MeV}$  data. To obtain the corrected cross sections, it is necessary to multiply all entries in Table 7 (page 55) and Table 13 (page 91) by 0.833, with the exception of those entries under the column headed  $E_n = 5.0 \text{ MeV}$ . In addition, the graphic displays of the data require a 17.7% ( $\times 0.833$ ) reduction of the data obtained at 8.0 to 11.0 MeV. Those figures requiring modification are found on the following pages: Figures 19-33 on pages 69-82, Figures 38-41 on pages 93-96, and Figure 42 on page 98. For convenience, corrected Tables 7 and 13 are reproduced on the following pages.

Table 7  
Experimental Differential Cross Sections for Gamma Rays from  $^{nat}\text{Si}(n,\text{Gr})$   
 $\sigma(55^\circ)$  (mb/sr)

$E_n$ (MeV)	5.00±0.10	8.00±0.15	9.00±0.15	10.00±0.15	11.00±0.15
$E_\gamma$ (MeV)					
<b>Discrete (a)</b>					
0.390		0.8±0.1	0.8±0.3	1.2±0.2 3.3±0.4	0.9±0.2
0.399		0.6±0.1	0.3±0.1		2.5±0.3
0.585		3.1±0.4	3.2±0.4		
0.759	0.3±0.1		0.3±0.1	0.6±0.2	0.7±0.2
0.856		1.7±0.3	0.8±0.2	1.0±0.2	0.9±0.2
0.942 (b) (0.98)		3.4±0.4	3.1±0.4	2.6±0.3	3.5±0.4
1.037	0.6±0.2	1.5±0.3	0.8±0.2	0.7±0.2	0.8±0.3
1.010		0.9±0.3	0.5±0.2	0.3±0.1	0.6±0.3
1.113					
(1.27)	1.5±0.2	2.2±0.4	1.5±0.3	1.4±0.3	1.7±0.3
1.341		0.8±0.3	0.7±0.2	0.5±0.2	1.2±0.3
1.380			0.8±0.2	1.1±0.3	1.0±0.3
(1.53)		2.7±1.2	1.8±0.8	2.8±0.8	4.6±1.2
(1.59) (c)		2.0±0.4	2.6±0.3	2.6±0.4	1.8±0.3
1.602 (c)					1.6±0.3
1.614		3.3±0.5	2.4±0.3	2.7±0.3	3.1±0.5
1.633		0.9±0.3	0.9±0.2	0.8±0.2	1.0±0.3
1.659 (d)		1.0±0.3	0.8±0.2	0.6±0.3	0.6±0.3
1.779	47.0±5.6	51.3±6.1	33.9±4.1	33.0±4.7	34.0±4.1
1.809		0.5±0.2	0.5±0.2	0.3±0.1	
1.963		0.3±0.2	0.6±0.2	0.8±0.3	0.6±0.3
2.032	1.0±0.2	1.8±0.3	0.8±0.3	1.0±0.2	1.4±0.3
2.203		0.6±0.2	1.6±0.3	1.3±0.3	1.8±0.3
2.232	1.3±0.2	2.0±0.3			
(2.27)					1.5±0.3
2.427	0.5±0.1				
2.838	1.0±0.2	8.7±1.1	4.7±0.6	3.7±0.5	5.6±0.8
3.196		2.7±0.4	2.7±0.3	0.9±0.3	0.9±0.3
4.497		3.6±0.6	3.2±0.5	2.5±0.4	1.9±0.4
4.911		1.7±0.6	1.4±0.3		
(5.10)		4.9±0.8	4.5±0.8	4.4±0.7	3.7±0.5
(5.60)		0.6±0.3	1.2±0.3	1.8±0.4	1.2±0.5
6.002			0.5±0.3		
6.019			0.5±0.3		
6.878		2.0±0.3	2.9±0.4	3.6±0.5	4.1±0.6
(7.40)		1.1±0.2	1.8±0.3	2.5±0.3	2.4±0.3
7.935			0.8±0.2	0.9±0.2	1.4±0.3
(8.30)				0.5±0.1	0.7±0.2
8.941				0.4±0.1	0.8±0.2
9.49					0.8±0.2
Total Discrete	53.2±6.4	106.7±16.0	82.2±12.4	79.8±12.0	89.3±13.4
Unresolved Continuum		8.8±1.3	17.7±2.7	24.1±3.6	38.6±5.8
Total Production (e)	53.2±6.4	115.5±17.3	100.6±15.1	103.9±15.6	127.9±19.2

- (a) Obtained for the most part with a Ge(Li) detector.
- (b) Gamma-ray energies in parentheses are average values for a group of unresolved lines.
- (c) The 1.614 MeV gamma ray and the group at 1.59 MeV may contain a small contribution from the unresolved 1.602 MeV gamma ray at neutron energies of 8.0, 9.0 and 10.0 MeV.
- (d) The 1.779 MeV gamma ray may contain minor contributions from the unresolved 1.763 and 1.796 MeV gamma rays. No real evidence of these gamma rays could be seen.
- (e) The total production cross section was obtained by adding the cross sections measured with the Ge(Li) detector for the discrete 0.390 and 0.399 MeV gamma rays to the total cross section for gamma rays of 0.55-11.0 MeV measured with the NaI(Tl) detector.

Table 13  
Experimental Differential Cross Sections for Gamma Rays  
from  $^{nat}W(n, G\gamma)$

		$\sigma(\theta)$ (mb/sr)				
$E_n$ (MeV)		5.0	8.0	9.0	10.0	11.0
	$\theta$	55°	(a)	125°	125°	125°
$E_\gamma$ (MeV)						
0.75-1.00		83.2 ±12.5	106.0 ±15.9	134.4 ±20.2	171.4 ±25.7	203.0 ±30.4
1.00-1.25		63.0 ±9.5	75.7 ±11.4	94.9 ±14.2	100.8 ±15.1	110.1 ±16.5
1.25-1.50		48.2 ±7.2	60.8 ±9.1	63.7 ±9.6	67.9 ±10.2	61.0 ±9.2
1.50-1.75		35.3 ±5.3	43.1 ±6.5	41.7 ±6.3	34.9 ±5.2	47.1 ±7.1
1.75-2.00		32.8 ±4.9	37.0 ±5.6	37.3 ±5.6	28.9 ±4.3	22.0 ±4.2
2.0-2.5		60.5 ±9.1	70.5 ±10.6	60.9 ±9.1	38.7 ±5.8	30.6 ±4.6
2.5-3.0		44.4 ±8.0	52.7 ±9.5	43.0 ±7.7	25.1 ±4.5	14.4 ±2.4
3.0-3.5		25.5 ±4.6	32.8 ±5.9	26.3 ±4.7	15.4 ±2.3	9.6 ±1.5
3.5-4.0		13.7 ±2.5	23.9 ±4.3	17.5 ±3.1	10.6 ±1.0	6.2 ±1.0
4.0-4.5		7.7 ±1.4	15.2 ±2.7	10.5 ±1.9	6.9 ±1.1	3.4 ±0.5
4.5-5.0		1.5 ±0.4	8.2 ±2.0	6.5 ±1.6	4.4 ±0.9	2.1 ±0.6
5.0-5.5			4.7 ±1.6	3.5 ±1.2	2.5 ±0.6	0.5 ±0.5
5.5-6.0			3.1 ±1.1	2.4 ±0.9	2.2 ±0.8	0.5 ±0.3
6.0-6.5				1.0 ±0.5	1.6 ±0.7	0.2 ±0.2

(a) Average of two 90° and one 125° runs.

THIS PAGE IS INTENTIONALLY LEFT BLANK.

DISTRIBUTION LIST

Copies

DEPARTMENT OF DEFENSE

1 DIRECTOR, ADVANCED RESEARCH PROJECTS AGENCY, ARCHITECT BUILDING,  
1111 W'LSON BLVD., ARLINGTON, VIRGINIA 22209  
ATTN: MR. FRED A. KOETHER, DIR. TECHNICAL INFO.

12 DEFENSE DOCUMENTATION CENTER, CAMERON STATION, ALEXANDRIA,  
VIRGINIA 22314  
ATTN: TC

1 DIRECTOR, DEFENSE INTELLIGENCE AGENCY, WASHINGTON, D.C. 20301  
ATTN: DI-78, PHYS. VUL. DIV., MR. EDWARD O'FARRELL

9 DIRECTOR, DEFENSE NUCLEAR AGENCY, WASHINGTON, D.C. 20305  
ATTN: APSI (ARCHIVES)  
ATTN: APTL, TECHNICAL LIBRARY (2)  
ATTN: RARP (5)  
ATTN: DDST

1 DIRECTOR OF DEFENSE RESEARCH & ENGINEERING, WASHINGTON, D.C. 20301

2 COMMANDER, FIELD COMMAND, DEFENSE NUCLEAR AGENCY, KIRTLAND AFB,  
NEW MEXICO 87115  
ATTN: TECHNICAL LIBRARY, FCTA-A  
ATTN: FCWD

1 CHIEF, LIVERMORE DIVISION, FIELD COMMAND, DNA, LAWRENCE LIVERMORE  
LABORATORY, P.O. BOX 808, LIVERMORE, CALIFORNIA 94550  
ATTN: FCWD-D

1 DIRECTOR, WEAPONS SYSTEMS EVALUATION GROUP, ODDR&E, OFFICE,  
SECRETARY OF DEFENSE, 400 ARMY-NAVY DRIVE, WASHINGTON, D.C. 20305  
ATTN: CPT DONALD E. MCCOY, USN

DEPARTMENT OF THE ARMY

5 COMMANDING OFFICER, ABERDEEN RESEARCH AND DEVELOPMENT CENTER,  
ABERDEEN PROVING GROUND, MARYLAND 21005  
ATTN: TECHNICAL LIBRARY, MR. EDWARD O. BAICY  
ATTN: AMXRD-BAM, DR. ARCHIE TEMPERLEY  
ATTN: AMXRD, DR. DONALD ECCLESALL  
ATTN: AMXRD-BNL, MR. DAVID L. RIGOTTI  
ATTN: AMXRD-BNL, EFFECTS ANALYSIS BRANCH

1 CHIEF OF RESEARCH & DEVELOPMENT, DEPARTMENT OF THE ARMY,  
WASHINGTON, D.C. 20310  
ATTN: ABMDA-CO

1 DEPARTMENT OF THE ARMY, HARRY DIAMOND LABORATORIES, WASHINGTON,  
D.C. 20438  
ATTN: AMXDO-NP

1 COMMANDING OFFICER, PICATINNY ARSENAL, DOVER, NEW JERSEY 07801  
ATTN: R. KESSELMAN

Copies

DEPARTMENT OF THE ARMY (CONTINUED)

1 COMMANDING OFFICER, SAFEGUARD SYSTEM EVALUATION AGENCY, WHITE SANDS MISSILE RANGE, NEW MEXICO 88002  
ATTN: EAB, R. E. DEKINDER, JR.

1 DIRECTOR, U.S. ARMY ADVANCED BALLISTIC MISSILE DEFENSE AGENCY, HUNTSVILLE OFFICE, P.O. BOX 1500, HUNTSVILLE, ALABAMA 35807

1 U.S. ARMY COMBAT DEVELOPMENTS COMMAND, NUCLEAR AGENCY, FORT BLISS, TEXAS 79916

1 COMMANDING GENERAL, U.S. ARMY ELECTRONICS COMMAND, FORT MONMOUTH, NEW JERSEY 07703  
ATTN: AMSEL-XL-D

1 COMMANDING GENERAL, U.S. ARMY MATERIEL COMMAND, WASHINGTON, D.C. 20315  
ATTN: AMCRD-BN-RE

DEPARTMENT OF THE NAVY

1 CHIEF OF NAVAL RESEARCH, DEPARTMENT OF THE NAVY, ARLINGTON, VIRGINIA 22217

3 COMMANDER, NAVAL ORDNANCE LABORATORY, SILVER SPRING, MARYLAND 20910  
ATTN: CODE 121, NAVY NUCLEAR PROGRAMS OFFICE  
ATTN: 1-315, TECHNICAL LIBRARY  
ATTN: DR. C. M. HUDDLESTON, CODE 223

1 SUPERINTENDENT, NAVAL POSTGRADUATE SCHOOL, MONTEREY, CALIFORNIA 93940  
ATTN: CODE 2124, TECHNICAL REPORTS LIBRARIAN

2 DIRECTOR, NAVAL RESEARCH LABORATORY, WASHINGTON, D.C. 20390  
ATTN: CODE 7633, DR. WAYNE D. JONES  
ATTN: CODE 7680, MR. LAVERNE S. BIRKS

1 COMMANDING OFFICER, NAVAL WEAPONS EVALUATION FACILITY, KIRTLAND AIR FORCE BASE, ALBUQUERQUE, NEW MEXICO 87117  
ATTN: J. ABBOTT

DEPARTMENT OF THE AIR FORCE

1 AF CAMBRIDGE RESEARCH LABORATORIES, AFSC, L. G. HANSCOM FIELD, BEDFORD, MASSACHUSETTS 01730  
ATTN: SUOL, AFCRL RESEARCH LIBRARY

1 AF INSTITUTE OF TECHNOLOGY, AU, WRIGHT-PATTERSON AFB, OHIO 45433  
ATTN: LIBRARY AFIT (I.D.), BUILDING 640, AREA B

1 CHIEF OF STAFF, U.S. AIR FORCE, WASHINGTON, D.C. 20330  
ATTN: OAS

1 COMMANDER, SPACE & MISSILE SYSTEMS ORGANIZATION (SAMSO), LOS ANGELES, CALIFORNIA 90045

Copies

DEPARTMENT OF THE AIR FORCE (CONTINUED)

6 AF WEAPONS LABORATORY, AFSC, KIRTLAND AFB, NEW MEXICO 87117  
ATTN: CHIEF, SR  
ATTN: SAA  
ATTN: SYT  
ATTN: DOGL, TECHNICAL LIBRARY  
ATTN: CHIEF, EST  
ATTN: CPT KIRK L. HALL

1 SPACE AND MISSILE SYSTEMS ORGANIZATION, AFSC, NORTON AFB, CALIFORNIA 92409  
ATTN: MMNSS, LTC CASMUS

ATOMIC ENERGY COMMISSION

1 ASSISTANT GENERAL MANAGER FOR MILITARY APPLICATION, U.S. ATOMIC ENERGY COMMISSION, WASHINGTON, D.C. 20545

4 LOS ALAMOS SCIENTIFIC LABORATORY, P.O. BOX 1663, LOS ALAMOS, NEW MEXICO 87544  
ATTN: DR. DONALD HARRIS  
ATTN: DOCUMENT CONTROL FOR MR. W. A. BIGGERS  
ATTN: DOCUMENT CONTROL FOR MR. D. R. WESTERVELT  
ATTN: DOCUMENT CONTROL FOR MR. D. R. THAYER

1 SANDIA LABORATORIES, LIVERMORE LABORATORY, P.O. BOX 969, LIVERMORE, CALIFORNIA 94550  
ATTN: DOCUMENT CONTROL FOR TECHNICAL LIBRARY

3 SANDIA LABORATORIES, P.O. BOX 5800, ALBUQUERQUE, NEW MEXICO 87115  
ATTN: DOC. CON. FOR ORG. 5230, DR. CLARENCE R. MEHL  
ATTN: DOC. CON. FOR ORG. 5231, DR. FRANK BIGGS  
ATTN: DOC. CON. FOR ORG. 3422-1, SANDIA RPTS COLL.

3 UNION CARBIDE CORPORATION, OAK RIDGE NATIONAL LABORATORY, P.O. BOX X, OAK RIDGE, TENNESSEE 37830  
ATTN: DOCUMENT CON. FOR DR. F. R. MYNATT  
ATTN: NEUTRON PHYSICS DIVISION, MR. C. E. CLIFFORD  
ATTN: DOCUMENT CONTROL FOR TECHNICAL LIBRARY

7 UNIVERSITY OF CALIFORNIA, LAWRENCE LIVERMORE LABORATORY, TECHNICAL INFORMATION DIVISION, P.O. BOX 808, LIVERMORE, CALIFORNIA 94550  
ATTN: T DIVISION, DR. T. WAINWRIGHT (2)  
ATTN: P DIVISION, DR. N. KEELER  
ATTN: B DIVISION, DR. W. GRAYSON  
ATTN: TECHNICAL LIBRARY  
ATTN: A DIVISION, DR. P. MOULTHROP  
ATTN: DR. ROBERT HOWERTON

OTHER GOVERNMENT

1 DEPARTMENT OF COMMERCE, NATIONAL BUREAU OF STANDARDS, CENTER FOR RADIATION RESEARCH, WASHINGTON, D.C. 20234  
ATTN: G. L. SIMMONS

Copies

DEPARTMENT OF DEFENSE CONTRACTORS

1 AEROSPACE CORPORATION, P.O. BOX 95085, LOS ANGELES, CALIFORNIA 90045  
ATTN: TECHNICAL LIBRARY

1 BATTELLE MEMORIAL INSTITUTE, 505 KING AVENUE, COLUMBUS, OHIO 43201  
ATTN: RADIATION EFFECTS INFORMATION CENTER

1 BELL TELEPHONE LABORATORIES, INC., MOUNTAIN AVENUE, MURRAY HILL,  
NEW JERSEY 07971  
ATTN: DR. N. BEAUCHAMP

1 THE BOEING COMPANY, P.O. BOX 3707; SEATTLE, WASHINGTON 98124

1 BRADDOCK, DUNN & MCDONALD, INC., P.O. BOX 10694, EL PASO, TEXAS 79925

1 BROWN ENGINEERING COMPANY, INC., RESEARCH PARK, HUNTSVILLE,  
ALABAMA 35807

1 GENERAL ELECTRIC COMPANY, TEMPO-CENTER FOR ADVANCED STUDIES,  
816 STATE STREET (P.O. DRAWER QQ), SANTA BARBARA, CALIFORNIA 93102  
ATTN: DASIAC

1 GULF OIL CORPORATION, P.O. BOX 1111, SAN DIEGO, CALIFORNIA 92112

1 INSTITUTE FOR DEFENSE ANALYSES, 400 ARMY-NAVY DRIVE, ARLINGTON,  
VIRGINIA 22202  
ATTN: TECHNICAL INFORMATION OFFICE

1 KAMAN SCIENCES CORPORATION, KAMAN NUCLEAR DIVISION, 1500 GARDEN OF  
THE GODS ROAD, COLORADO SPRINGS, COLORADO 80907  
ATTN: DR. FRANK H. SHELTON

2 LOCKHEED MISSILES AND SPACE COMPANY, 3251 HANOVER STREET, PALO ALTO,  
CALIFORNIA 94304  
ATTN: DR. LLOYD F. CHASE, DEPT. 52-11, BLDG. 203  
ATTN: TECHNICAL LIBRARY

1 LOCKHEED MISSILES AND SPACE COMPANY, DIVISION OF LOCKHEED AIRCRAFT  
CORPORATION, P.O. BOX 504, SUNNYVALE, CALIFORNIA 94088  
ATTN: LIBRARY

1 MARTIN MARIETTA CORPORATION, ORLANDO DIVISION, P.O. BOX 5837,  
ORLANDO, FLORIDA 32805

2 MATHEMATICAL APPLICATIONS GROUP, INC., 3 WESTCHESTER PLAZA,  
ELMSFORD, NEW YORK 10523  
ATTN: DR. HERB STEINBERG  
ATTN: DR. MALVIN KALOS

1 MCDONNELL DOUGLAS CORPORATION, 3000 OCEAN PARK BLVD., SANTA MONICA,  
CALIFORNIA 90406

1 MCDONNELL DOUGLAS CORPORATION, 5301 BOLSA AVENUE, HUNTINGTON BEACH,  
CALIFORNIA 92647  
ATTN: A3-328, TECHNICAL LIBRARY SERVICES

Copies

DEPARTMENT OF DEFENSE CONTRACTORS (CONTINUED)

1 MISSION RESEARCH CORPORATION, 1 PRESIDIO AVENUE, SANTA BARBARA,  
CALIFORNIA 93101  
ATTN: DR. CONRAD LONGMIRE

1 THE MITRE CORPORATION, ROUTE 62 AND MIDDLESEX TURNPike, P.O. BOX  
208, BEDFORD, MASSACHUSETTS 01730  
ATTN: TECHNICAL LIBRARY

1 NORTH AMERICAN ROCKWELL CORPORATION, AUTONETICS, ELECTRONICS  
GROUP, 3370 MIRALOMA AVENUE, ANAHEIM, CALIFORNIA 92803  
ATTN: TECHNICAL LIBRARY

1 PHYSICS INTERNATIONAL COMPANY, 2700 MERCED STREET, SAN LEANDRO,  
CALIFORNIA 94577  
ATTN: DOCUMENT CON. FOR SENIOR LIBRARIAN

3 R & D ASSOCIATES, P.O. BOX 3580, SANTA MONICA, CALIFORNIA 90403  
ATTN: DR. HAROLD L. BRODE  
ATTN: MR. WILLIAM B. WRIGHT, JR.  
ATTN: DR. WILLIAM J. KARZAS

1 RADIATION RESEARCH ASSOCIATES, INC., 3550 HULEN STREET, FORT WORTH,  
TEXAS 76107  
ATTN: LIBRARY

1 SCIENCE APPLICATIONS, INC., P.O. BOX 2351, LA JOLLA, CALIFORNIA 92037  
ATTN: DR. J. ROBERT BEYSTER, PRESIDENT

1 SCIENCE APPLICATIONS, INC., HUNTSVILLE OFFICE, 2109 W. CLINTON AVENUE,  
SUITE 700, HUNTSVILLE, ALABAMA 35805

1 STANFORD RESEARCH INSTITUTE, 333 RAVENSWOOD AVENUE, MENLO PARK,  
CALIFORNIA 94025  
ATTN: MR. ARTHUR WHITSON

1 SYSTEMS, SCIENCE AND SOFTWARE, INC., P.O. BOX 1620, LA JOLLA,  
CALIFORNIA 92037  
ATTN: TECHNICAL LIBRARY

1 TENNECOMP, INC., P.O. BOX J, OAK RIDGE, TENNESSEE 37830  
ATTN: MR. WALTER R. BURRUS

2 TRW SYSTEMS GROUP, ONE SPACE PARK, REDONDO BEACH, CALIFORNIA 90278  
ATTN: DR. ROBERT WEBB  
ATTN: DR. BENJAMIN SUSSHOLTZ

1 UNIVERSITY OF WISCONSIN, NUCLEAR ENGINEERING DEPARTMENT, MADISON,  
WISCONSIN 53706  
ATTN: DR. HAROLD K. FORSEN

MISCELLANEOUS

1 DEFENCE RESEARCH BOARD, DEFENCE RESEARCH ESTABLISHMENT, OTTAWA,  
OTTAWA 4, ONTARIO, CANADA  
ATTN: DR. C. E. CLIFFORD

THIS PAGE IS INTENTIONALLY LEFT BLANK.